Sofia Goldbach d'Orsi

U-Pb E Lu-Hf EM ZIRCÕES DETRÍTICOS DOS PARAGNAISSES DO TERRENO ORIENTAL – CIDADE DO RIO DE JANEIRO

Trabalho Final de Curso

(Geologia)

UFRJ
Rio de Janeiro
2024

UFRJ

Sofia Goldbach d'Orsi

U-Pb E Lu-Hf EM ZIRCÕES DETRÍTICOS DOS PARAGNAISSES DO TERRENO ORIENTAL – CIDADE DO RIO DE JANEIRO

Trabalho Final de Curso de Graduação em Geologia do Instituto de Geociências, Universidade Federal do Rio de Janeiro – UFRJ, apresentado como requisito necessário para obtenção do grau de Geólogo.

Orientadores:

Profª. Dra. Renata da Silva Schmitt
(Depto. Geologia, IGEO/UFRJ)

Profª. Dra. Silvia Regina de Medeiros
(Depto. Geologia, IGEO/UFRJ)

Prof. Dr. Mauro Cesar Geraldes
(Faculdade de Geologia, UERJ)

Rio de Janeiro

Outubro de 2024

D'ORSI, Sofia Goldbach

U-Pb E Lu-Hf EM ZIRCÕES DETRÍTICOS DOS PARAGNAISSES DO TERRENO ORIENTAL – CIDADE DO RIO DE JANEIRO/ Sofia Goldbach d'Orsi - Rio de Janeiro: UFRJ / IGeo, 2024.

xi, 61 p.

Trabalho de conclusão de curso (graduação) – Universidade Federal do Rio de Janeiro, Instituto de Geociências, Departamento de Geologia, 2024.

Orientadora: Renata da Silva Schmitt;

Coorientadores: Silvia Regina de Medeiros; Mauro Cesar Geraldes

1. Geologia. 2. IGEO - Trabalho de Conclusão de Curso. I. Renata da Silva Schmitt, UFRJ. II. Universidade Federal do Rio de Janeiro, Instituto de Geociências, Departamento de Geologia. III. U-Pb e Lu-Hf em zircões detríticos dos paragnaisses do Terreno Oriental - cidade do Rio de Janeiro.

Sofia Goldbach d'Orsi

U-Pb E Lu-Hf EM ZIRCÕES DETRÍTICOS DOS PARAGNAISSES DO TERRENO ORIENTAL – CIDADE DO RIO DE JANEIRO

Trabalho Final de Curso de Graduação em Geologia do Instituto de Geociências, Universidade Federal do Rio de Janeiro – UFRJ, apresentado como requisito necessário para obtenção do grau de Geólogo.

Orientadores:

Profª. Dra. Renata da Silva Schmitt
(Depto. Geologia, IGEO/UFRJ)

Profª. Dra. Silvia Regina de Medeiros
(Depto. Geologia, IGEO/UFRJ)

Prof. Dr. Mauro Cesar Geraldes
(Faculdade de Geologia, UERJ)

Aprovada em:

Por:

_____
Orientador: Profª. Dra. Renata da Silva Schmitt (UFRJ)

_____
Profª. Dra. Beatriz Paschoal Duarte (UERJ)

_____
Dr. Guilherme Gonçalves Martins (UFRJ)

UFRJ
Rio de Janeiro
Outubro de 2024

"O segredo está aqui no presente. Se você prestar atenção ao presente, poderá melhorá-lo. E, se você melhorar o presente, o que virá depois também será melhor."

- Paulo Coelho (O Alquimista)

AGRADECIMENTOS:

Agradeço primeiramente ao apoio financeiro da Petrobrás/CENPES em cooperação com a UFRJ através do projeto "Geodinâmica da litosfera continental do Gondwana SW - o embasamento do sistema de riftes do Atlântico Sul". Assim como aos recurso obtidos junto à FAPERJ de "Apoio as Instituições de Pesquisa Sediadas no RJ" (E-26/010.101120/2018). Agradeço também ao laboratório Centro Digital de Geoprocessamento Gondwana por todo apoio de estrutura necessária para a confecção do trabalho e pelos colegas com tantos bons conselhos.

Às minhas orientadoras Renata e Silvia, agradeço por sempre acreditarem no projeto e me incentivarem a ir cada vez mais longe. Sou muito agradecida por cada ensinamento que me foi passado e por cada reunião enriquecedora que tivemos. Obrigada por serem um exemplo inspirador de mulheres e pesquisadoras nas Geociências.

Ao coorientador e colaborador Mauro Cesar Geraldes, pela disponibilidade e apoio com o trabalho.

Aos colegas que participaram diretamente desse trabalho Rodrigo Gentil Coelho de Azambuja, Thayla Almeida Teixeira Vieira, Mateus da Silva Ferreira e João Victor Sampaio Abreu pela colaboração.

Ao corpo de professores da Geologia UFRJ por todo aprendizado e pelas valiosas lições durante esses anos de graduação. Agradeço o constante interesse e participação que demonstram no dia a dia e por estarem sempre dispostos a ajudar como sendo verdadeiras "vozes da experiência". Em especial ao professor André Ribeiro, sou extremamente grata por todas as conversas e histórias desde minha entrada na UFRJ.

Aos meus inúmeros amigos e colegas de curso por estarem ao meu lado e compartilharem essa experiência comigo. Sobretudo à Amanda Mendes por ser meu suporte e minha eterna dupla.

Por fim, agradeço imensamente aos meus pais, Ricardo e Myriam, pelo carinho, cuidado e paciência durante essa longa jornada. Às minhas primas, Iris e Nina, pela incansável celebração de todas as pequenas conquistas. Á toda minha família pelo apoio. E aos geólogos que desde cedo fizeram parte da minha vida: Luís Otávio Oliveira, João Pedro Oliveira, Frederico Sobreira, Ricardo Siqueira, Ricardo Rúbio P. Alves, e meus queridos pais Ricardo d'Orsi e Myriam d'Orsi.

RESUMO

D'ORSI, Sofia Goldbach. **U-Pb E Lu-Hf EM ZIRCÕES DETRÍTICOS DOS PARAGNAISSES DO TERRENO ORIENTAL – CIDADE DO RIO DE JANEIRO**. 2024. xi, 59 f. Trabalho Final de Curso (Geologia) – Departamento de Geologia, Instituto de Geociências, Universidade Federal do Rio de Janeiro, Rio de Janeiro.

Durante a convergência dos paleocontinentes São Francisco e Congo-Angola, entre 600 e 500 Ma, bacias sedimentares foram geradas, e seus registros estão parcialmente preservados nos paragnaisses do Orógeno Ribeira. Nesta faixa orogênica, o Terreno Oriental é constituído majoritariamente por paragnaisses intrudidos por volumosos batólitos pré-, sin- e pós-colisionais. Aqui investigamos a origem dos paragnaisses que afloram na cidade do Rio de Janeiro (Brasil). O Grupo São Fidélis é composto principalmente por cordierita-sillimanita-granada-biotita paragnaisses, com intercalação de camadas de quartzito. As condições de pico metamórfico são 750–800°C e abaixo de 7 kbar dentro da fácies granulito. Nosso objetivo é realizar a análise de proveniência dos protólito sediementares e investigar a evolução tectônica da bacia, dado que esta unidade passou por metamorfismo de alta temperatura acima da temperatura de fechamento do sistema U-Pb em zircão. A metodologia combinou análises U-Pb e Lu-Hf. O trabalho de campo foi realizado na Avenida Niemeyer e no Morro Cara de Cão. Três amostras de litologias distintas foram analisadas: cordierita-sillimanita-granada-biotita paragnaisse (kinzigito), biotita-paragnaisse fino e quartzito micáceo. Os dados mostram que todas as litologias têm um padrão semelhante de distribuição das idades de zircão detrítico. As principais populações neoproterozoicas são: 980-930 Ma, 856-838 Ma, 800-740 Ma e 690-580 Ma. Os picos coincidem com as idades dos arcos magmáticos descritos no Terreno Oriental, sugerindo-os como fontes. Uma população de zircão mais jovem, na faixa de 570-550 Ma, pode ser interpretada como metamórfica ou magmática, devido às incertezas causadas por perda de Pb. Populações detríticas secundárias mesoproterozoicas e paleoproterozoicas podem ter origem no Complexo Anortosítico Kunene e nas unidades magmáticas eburneanas do Cráton de Angola e do Domínio Tectônico de Cabo Frio. Os valores de εHf neoproterozoicos para os grãos datados variam de +5 a -18, sendo compatível com fontes mantélicas e crustais, presentes em arcos magnéticos. Com base na idade do zircão detrítico mais jovem, a idade mínima deposicional para a bacia é calculada como 570 Ma, corroborada pela idade de cristalização da unidade Ortognaisse Facoidal, intrusiva nos paragnaisses. O curto intervalo entre o metamorfismo e a deposição nessa bacia sugere que se trata de uma bacia sin-orogênica, provavelmente de retroarco ou antearco, e, portanto, o metamorfismo seria atribuído a uma anomalia térmica regional relacionada ao orógeno quente.

Palavras-chave: Paragnaisses, geocronologia U-Pb, sistema Lu-Hf, Faixa Ribeira, orógeno quente.

ABSTRACT

D'ORSI, Sofia Goldbach. **U-Pb AND Lu-Hf IN DETRITAL ZIRCONS FROM THE PARAGNEISSES OF THE ORIENTAL TERRANE – RIO DE JANEIRO CITY**. 2024. xi, 59 f. Trabalho Final de Curso (Geologia) – Departamento de Geologia, Instituto de Geociências, Universidade Federal do Rio de Janeiro, Rio de Janeiro.

During the convergence of the São Francisco and the Congo-Angola paleocontinents, between 600 and 500 Ma, sedimentary basins were generated and their record is preserved in paragneisses, within the Ribeira Orogen. This orogenic belt presents the Neoproterozoic arc Oriental Terrane, mostly constituted by paragneisses intruded by voluminous batholiths pre-, syn- and post-collisional. Here we investigate the origin of the paragneisses that crop out in the Rio de Janeiro city (Brazil). The São Fidélis Group consists mostly of cordierite-sillimanite-garnet-biotite paragneisses with minor quartzite layers at. Peak metamorphic conditions were 750–800°C below 7 kbar. Our goal is to study the provenance of the sedimentary protoliths and the basin's tectonic evolution, as this unit underwent high-temperature metamorphism above the zircon closure temperature for the U-Pb system. The methodology combined zircon U-Pb and Lu-Hf analyses. Fieldwork was conducted at Niemeyer Avenue and Morro Cara de Cão. Three samples from distinct lithologies were analysed: cordierite-sillimanite-garnet-biotite paragneiss (kinzigite), fine-grained biotite paragneiss, and micaceous quartzite. Data shows that all lithologies have a similar pattern of distribution for detrital zircon populations. The main Neoproterozoic populations are: 980-930 Ma, 856-838 Ma, 800-740 Ma and 690-580 Ma. The peaks coincide with the ages of the magmatic arcs described in the Oriental Terrane, suggesting them as sources. The youngest zircon population of 570-550 Ma could be either interpreted as metamorphic or magmatic, due to Pb-loss uncertainties. Minor Mesoproterozoic and Paleoproterozoic detrital populations might source from the Kunene Anorthosite Complex and the Eburnean magmatic units of the Angola Craton and the Cabo Frio Tectonic Domain. The Neoproterozoic εHf values for the dated detrital zircons range from +5 to -18, compatible with mantle and crustal sources, present in magmatic arcs. The youngest detrital zircon and minimal depositional age for the basin is calculated as 570 Ma, supported by the crystallisation age of the Facoidal Orthogneiss unit, intrusive in the paragneisses. The short interval between metamorphism and deposition indicates that this was a syn-orogenic basin, probably a back-arc or forearc and therefore the metamorphism would be attributed to a regional thermal anomaly related to a hot-orogen.

Key-Words: Paragneiss, U-Pb geochronology, Lu-Hf system, Ribeira Belt, Hot-orogen.

LISTA DE FIGURAS DA MONOGRAFIA

LISTA DE FIGURAS DO ARTIGO

SUMÁRIO

I. INTRODUÇÃO

A geocronologia de zircões detríticos é amplamente utilizada para desvendar a evolução tectônica de bacias sedimentares (Kelly e Harley, 2005; Gehrels, 2014; Condie *et al.*, 2017; Barham *et al.*, 2022). Este método baseia-se na obtenção das idades de cristalização de grãos de zircão presentes no preenchimento sedimentar da bacia estudada, obtendo assinaturas de idade das áreas de onde esses grãos foram originalmente erodidos antes de se depositarem na bacia, permitindo caracterizá-los como "zircão detrítico". Com base nessas assinaturas, é possível correlacionar as idades dos zircões às áreas-fonte e associá-las a terrenos cronologicamente compatíveis, sugerindo, assim, quais terrenos contribuíram para o processo de formação da bacia.

No entanto, há uma limitação significativa para esta metodologia quando trabalhando em bacias formadas em antigos cinturões orogênicos, especialmente quando com gradientes geotérmicos elevados. Embora o zircão seja altamente eficaz em preservar a idade de formação através do sistema isotópico U-Pb, sua precisão pode ser afetada pela interferência de metamorfismo de alta temperatura (Zheng *et al.*, 2005; Harley *et al.*, 2007). Em temperaturas acima de 700-750 °C, o sistema pode abrir, ter perda de chumbo e ser reiniciado (Rubatto *et al.,* 2001; Moecher e Samson, 2006; Gehrels, 2011; Tedeschi *et al.,* 2023). Além disso, em ambientes convergentes tectonicamente ativos, surge uma dificuldade adicional: a rápida taxa dos processos tectônicos pode aproximar as idades de sedimentação e metamorfismo a um intervalo similar, dentro das margens de erro (Cawood *et al.*, 2012; Jian *et al.*, 2022), dificultando a interpretação dos dados.

Neste trabalho, abordamos este desafio para avaliar a influência do metamorfismo de alta temperatura ao usar essa e outras evidências geológicas para inferir a idade das rochas fonte da bacia estudada e sua evolução tectônica, desde a sedimentação até o metamorfismo.

Três amostras dos paragnaisses da cidade do Rio de Janeiro, pertencentes ao Terreno Oriental - um domínio interpretado como um orógeno quente da Faixa Ribeira no sudeste do Brasil (Bento dos Santos *et al.,* 2015; Valeriano *et al.,* 2016) - foram estudadas com uso da geocronologia U-Pb combinada com o método Lu-Hf para uma compreensão mais abrangente da idade e origem da bacia sedimentar que serviu como protólito desses gnaisses de alta temperatura (750–800°C) e média pressão (7 kbar) (Kuhn *et al.* 2004).

i. Objetivos

O objetivo deste trabalho é aprofundar o entendimento acerca da evolução tectônica das bacias orogênicas neoproterozoicas do Domínio Costeiro (Terreno Oriental, Orógeno Ribeira) por meio da investigação isotópica dos paragnaisses aflorantes na cidade do Rio de Janeiro. Para isso, foram realizadas análises U-Pb e Lu-Hf em cristais de zircão detrítico para o estudo de proveniência das rochas paraderivadas do Grupo São Fidélis. Visando, assim, compreender a área fonte dos sedimentos e o ambiente tectônico dessas bacias sedimentares pré-colisionais. A finalidade é contribuir com o entendimento da dinâmica de sedimentos no Domínio Costeiro da Faixa Ribeira e sua relação com os terrenos magmáticos durante a orogenia Brasiliana-Pan-Africana.

ii. Justificativa

O presente trabalho sobre cristais de zircão detrítico nas rochas paraderivadas aflorantes no Rio de Janeiro visa suprir a lacuna de dados dessas rochas na cidade. O quartzito micáceo que aflora ao longo da Avenida Niemeyer não havia sido analisado em detalhes até a realização deste estudo. A investigação desse quartzito permitirá compreender sua gênese e idade, contribuindo assim para o entendimento da geologia local.

Nos últimos anos, estudos semelhantes de U-Pb em zircão detrítico têm sido realizados em paragnaisses do Grupo São Fidélis (assim como das sucessões Búzios e Palmital no Domínio Tectônico de Cabo Frio) com o objetivo de aprimorar o modelo evolutivo do Terreno Oriental – Faixa Ribeira. Diferentes projetos dataram essas rochas em regiões mais ao N-NE do estado do Rio de Janeiro, e os resultados indicam pequenas variações conforme a localização da amostra na sequência meta-sedimentar. O presente trabalho foi desenvolvido em uma área ainda não explorada por outros autores, o que pode destacar diferenças e/ou novas fontes que anteriormente não haviam sido identificadas, revelando novos intervalos de idade para a deposição do Grupo São Fidélis.

Por fim, a existência prévia de informações sobre o metamorfismo no paragnaisse kinzigito na cidade do Rio de Janeiro despertou interesse em relação à idade de deposição dos sedimentos que formaram essa rocha. A possibilidade de integrar dados de P-T-t do metamorfismo com a idade máxima de deposição do kinzigito proporciona uma interpretação mais aprofundada da evolução da geologia da região.

iii. Localização e acesso

Figura 1 – Mapa de localização no Brasil. Estado do Rio de Janeiro indicado em vermelho. Cidade do Rio de Janeiro indicada com estrela preta.

A área estudada localiza-se na cidade do Rio de Janeiro, estado do Rio de Janeiro, Brasil (Figura 1). A região escolhida para o trabalho de campo é delimitada pela Zona Sul do Rio de

Janeiro (RJ) (Fig. 2). No entanto, os trabalhos de campo foram realizados em dois afloramentos rochosos específicos: Morro Cão de Cão (Urca) (Figura 2) e costão ao lado de uma porção da Avenida Niemeyer (Vidigal) (Figura 3).

No Morro Cara de Cão, a parte vista em campo foi na face nordeste. Os afloramentos de onde foram coletadas as amostras foram restritos ao acesso pelo caminho do Museu Histórico da Fortaleza de São João.

Figura 2 – Imagem de satélite da região da Urca, Rio de Janeiro (Google Earth), destacando o trecho de trabalho de campo no Morro Cara de Cão.

Na Avenida Niemeyer, a porção específica em que ocorreu o trabalho de campo, foram os afloramentos situados no trecho entre o Sheraton Grand Rio Hotel & Resort (Av Niemeyer, nº 121) e o chamado Mirante do Leblon (aproximadamente Av Niemeyer nº 3, Vidigal).

Figura 3 – Imagem de satélite da região do Vidigal, Rio de Janeiro (Google Earth), destacando o trecho de trabalho de campo ao longo da Avenida Niemeyer.

iv. Estrutura da monografia

Esta monografia adota um formato estruturado em torno da apresentação de um artigo científico. Embora trate dos mesmos tópicos de uma monografia tradicional, esses tópicos são elaborados de forma mais concisa. Os principais resultados e discussões estão consolidados no artigo, ainda com título provisório, "U-Pb and Lu-Hf Zircon Analysis in a Hot-Orogen: Oriental Terrane, Rio de Janeiro", preparado para publicação em uma revista científica ainda não definida (página 23). Neste formato, uma seção de materiais e métodos mais detalhada foi incluída para esclarecer o passo-a-passo realizado pela autora.

No corpo da monografia, figuras são referenciadas de dois modos distintos. “Figura *X*” é relativo a figuras inclusas apenas na monografia/TCC (em português). “Fig. *Y*” é relativo a figuras (“*Figures*”) do artigo elaborado (em inglês).

II. MATERIAIS E MÉTODOS

Os métodos e técnicas utilizados no presente trabalho, bem como os procedimentos laboratoriais de preparação e análise de amostras, são apresentados nesse tópico.

A metodologia contou primeiramente com um estudo bibliográfico (Figura 4) para um entendimento prévio da geologia local do município do Rio de Janeiro. O foco foi a melhor compreensão da relação geológica entre as rochas aflorante na cidade, em especial as rochas para-derivadas do Grupo São Fidélis. A partir da revisão bibliográfica foi possível selecionar locais-chave de interesse do projeto, em que esse grupo aflora. Em seguida, foram utilizadas imagens de satélite Google Earth e Google Maps para determinar os afloramentos que fossem viáveis para a realização de trabalho de campo (Figura 4).

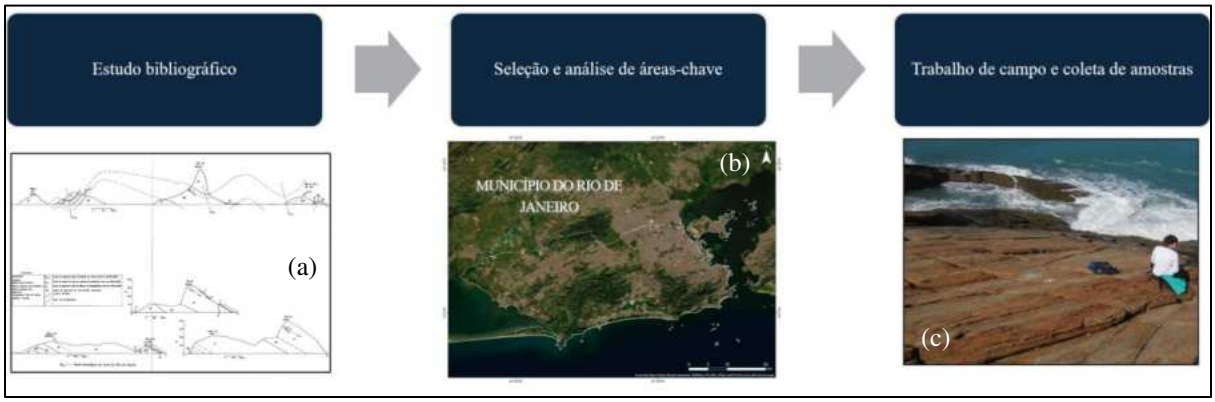

Figura 4 – Fluxograma ilustrativo de metodologia com as etapas iniciais: Estudo bibliográfico; Seleção e análise de áreas-chave; Trabalho de campo e coleta de amostras. (a) Perfis geológicos da área do Pão de Açúcar (Valeriano e Magalhães, 1984). (b) Imagem de satélite Google Earth com delimitação do município do Rio de Janeiro. (c) Foto de campo no afloramento Avenida Niemeyer.

A próxima etapa foi a realização dos trabalhos de campo no Morro Cara de Cão (Urca) (Figura 2) e na Avenida Niemeyer (Vidigal) (Figura 3). Foram feitas coletas de amostras com objetivo de datação geocronológica e de descrição litológica em lâmina delgada. No Morro Cara de Cão, foram coletadas 6 amostras no total, sendo 2 para geocronologia (CC_05A e CC_03B). Na Avenida Niemeyer, foram coletadas 5 amostras no total, sendo 1 para geocronologia (Ni_01). Durante o procedimento de coleta, veios pegmatíticos foram evitados e as rochas coletadas não se apresentavam intemperizadas. Foram gerados um mapa geológico de detalhe e uma seção geológica com os dados de campo para cada área.

As três amostras selecionadas para análises geocronológicas pelo método LA-ICP-MS passaram por diversos procedimentos em laboratório. Os laboratórios envolvidos na preparação das amostras para concentração de zircão foram o Laboratório de Amostras Geológicas (LAG) do Departamento de Geologia da UFRJ e o Laboratório Geológico de Processamento de

Amostras (LGPA) do Departamento de Geologia da UERJ. A técnica analítica LA-ICP-MS (Laser Ablation – Inductively Coupled Plasma – Mass Spectrometry) foi realizada no Laboratório Multiusuário de Meio Ambiente e Materiais (MultiLab) do Departamento de Geologia da UERJ. A etapa de tratamento de dados foi realizada no Centro Digital de Geoprocessamento Gondwana (CDGG) do Departamento de Geologia da UFRJ.

A preparação seguiu o fluxograma de preparação das amostras para geocronologia que visa à concentração mineral para separação de cristais de zircão (Figura 5).

Figura 5 – Fluxograma ilustrativo de metodologia com as etapas laboratoriais de concentração de zircão: Britador; Moinho de disco; Bateia; Imã de mão; Líquido denso (iodeto de metileno); Frantz (Separação magnética).

Após a lavagem e secagem em estufa, as amostras foram processadas em um britador de mandíbulas, reduzindo o material a uma fração de até 2 mm. Em seguida, o material foi fragmentado em moinho de discos até atingir cristais com granulometria de 200 mesh. O material mais denso foi concentrado com o uso de bateia. Os minerais magnéticos (magnetita), foram removidos utilizando um ímã de mão. O concentrado foi submetido à separação densimétrica em líquido denso iodeto de metileno de densidade 3,325 g/cm³, resultando em uma fração leve e uma fração pesada contendo o zircão (densidade 4,6 g/cm³). O material foi colocado no separador magnético Frantz, uma vez que o zircão é um mineral diamagnético, ou seja, não é atraído. As amperagens utilizadas no Frantz foram: 0,3 A, 0,4 A, 0,8 A, 1,0 A e 1,5 A. Então, os grãos de zircão foram coletados manualmente com auxílio de lupa binocular e organizados em mounts em epóxi. Esses mounts contendo o zircão foram polidos e depois imageados através do MEV gerando imagens de catodoluminescência e backscatter (elétrons

retro-espalhados) (Figura 6). Os locais escolhidos em cada grão para a serem analisados para U-Pb foram marcados nessas imagens, evitou-se grãos com fissuras ou muito danificados.

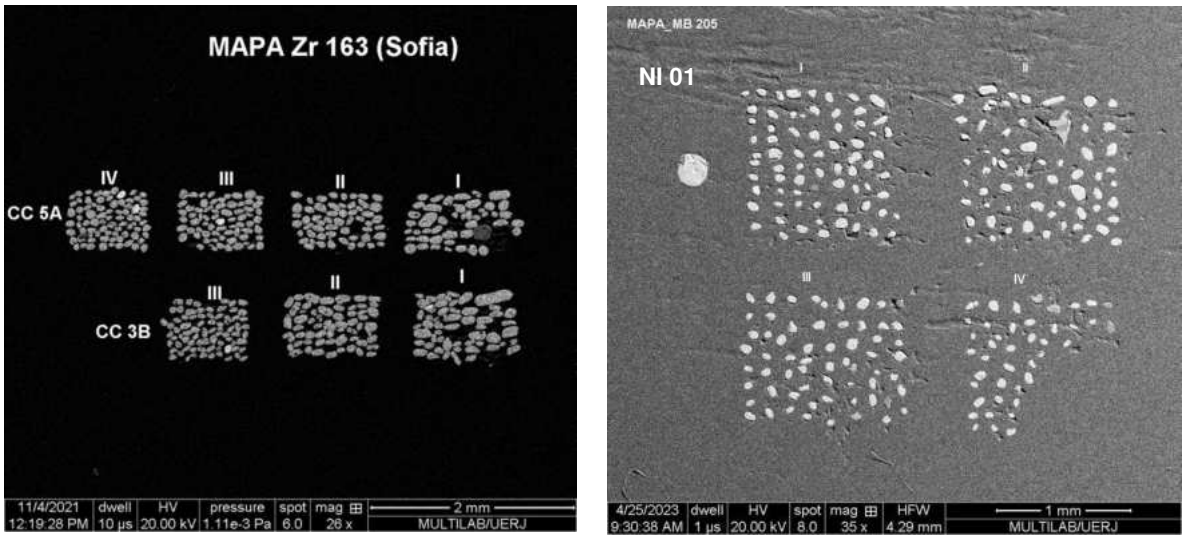

Figura 6 – Imageamento dos mounts contendo grãos zircão das três amostras (MULTILAB-UERJ).

Em seguida foram realizadas as análises utilizando Laser Ablation – MC-ICP-MS Neptune (termo Finnigan) (espectrometria de massa por ablação a laser acoplada a plasma indutivamente acoplado com múltiplos coletores) do MULTILAB-UERJ (Figura 7), um multicoletor de alta resolução com 9 coletores Faraday e 6 contadores de íons. O LA-ICP-MS é subdividido em fonte, separador, detector e registrados. O equipamento faz a leitura de concentrações dos isótopos dos elementos que foram volatizados por laser ablation em cristais de zircão. O mount é colocado no compartimento reservado, juntamente com as amostras padrão para calibração. A sequência de aquisição de dados começa com a seleção do grão a ser analisado e a escolha do local onde o tiro será feito, previamente determinados com o auxílio das imagens. Em seguida, aciona-se o feixe de laser para iniciar a ablação, e a coleta de dados constitui em 50 ciclos de 1 segundo.

Para o método U-Pb, utilizou-se as amostras padrão GJ-1 e 91500. A ablação foi feita com um feixe de 40 micrômetros, a uma frequência de 6 Hz e uma intensidade de 8 mJ. O carreamento foi feito som um fluxo de hélio de 0,5 L/min. Foram realizadas 120 medições de idade U-Pb em zircão para cada uma das três amostras.

Com os grãos previamente analisados com U-Pb, foram selecionados os cristais de zircão em que seria feita a medição Lu-Hf. A escolha levou em consideração a qualidade adequada na margem de erro das idades já obtidas e, também, a área restante do grão para ablação. As medições foram feitas em um total de 60 grãos divididos em duas amostras

(CC_5A e CC_3B). As calibrações utilizaram os padrões GJ-01, 91500 e MudTank. Os tiros foram de 40 micrômetros a uma frequência de 10 Hz.

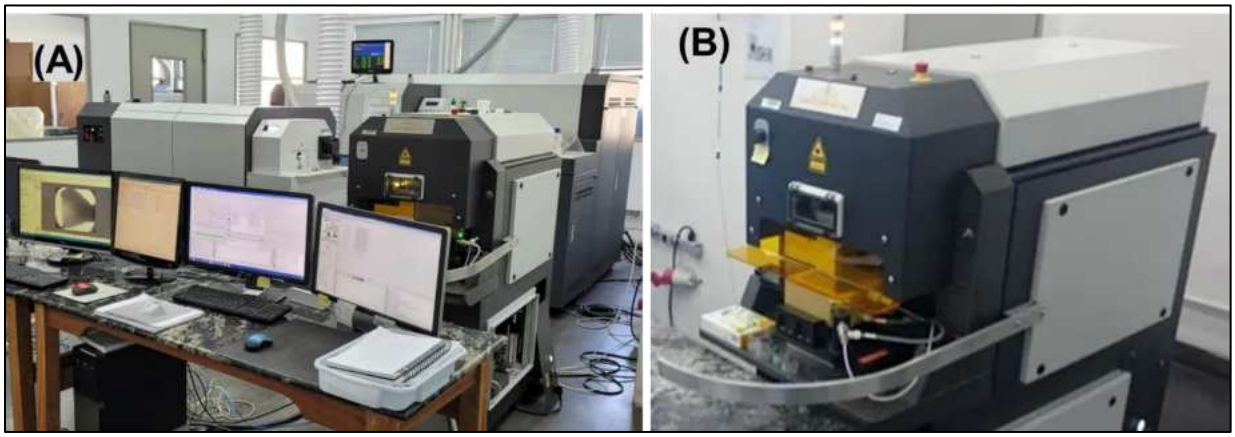

Figura 7 – Fotografias: (A) Equipamento utilizado no MULTILAB-UERJ; e (B) Neptune plus LA- ICP-MS. Fonte: Disponível em: <https://multilab-uerj.com.br/>, 2024 (acessado em 10/10/2024 às 15:00 horas).

III. GEOLOGIA LOCAL

i. Morro Cara de Cão

Durante o trabalho de campo na região do Morro Cara de Cão (Fig. 4a), foram identificadas três litologias principais: ortognaisse facoidal, cordierita-granada-biotita paragnaisse migmatítico e biotita paragnaisse fino.

O ortognaisse facoidal aflora em grande parte da área mapeada, sendo caracterizado como um ortognaisse porfirítico de coloração variando do cinza claro ao escuro, com fenocristais que vão do esbranquiçado ao rosado. A granulação da matriz é fina a média, enquanto os porfiroclastos são grossos a muito grossos, podendo atingir até 5 cm de comprimento. A mineralogia é composta por quartzo, K-feldspato, plagioclásio e biotita, com a presença ocasional de granada, especialmente nos leucossomas. A foliação principal é marcada pela biotita e pelos porfiroclastos. Esses porfiroclastos orientados são predominantemente de K-feldspato e ocasionalmente plagioclásios e possuem formato tabular a ovalado (*augen*).

O cordierita-granada-biotita paragnaisse migmatítico ocorre em contato brusco com o ortognaisse facoidal (intrusivo). Localmente, é observado um paragnaisses fino dentro do cordierita-granada-biotita paragnaisse próximo ao contato com o ortognaisse. Possui granulação média a grossa, e sua mineralogia é quartzo, biotita, granada e plagioclásio. Ele é caracterizado por um bandamento composicional que evidencia níveis de fusão parcial, permitindo a clara distinção entre as porções leucossomáticas e melonossomáticas. Exibe

migmatização (estromática), com textura marcada por porfiroblastos de granada de até 3 cm. Localmente apresenta dobras intrafoliais.

O biotita-paragnaisse fino aflora em uma lente de cerca de 30 cm, localizada próxima ao contato entre o ortognaisse facoidal e o cordierita-granada-biotita paragnaisse migmatítico. Este é caracterizado como um gnaisse homogêneo, de coloração escura e granulação fina a muito fina.

Em campo, foram feitas medidas estruturais de estruturas dúcteis caracterizadas como Sn (foliação), referindo-se à primeira fase de deformação encontrada na região. As medidas de foliação tectônica principal, tanto das rochas paraderivadas quanto no ortognaisse, indicam um baixo a médio ângulo de mergulho Sul. Medidas de lineação de estiramento (Le) mergulham para sudoeste, variando de 220° a 240°, com ângulo de mergulho médio de 45°. No ponto mais para sul da área mapeada, foi encontrado uma foliação para leste com ângulo de mergulho médio de 50° e lineação de estiramento para nordeste (060°) com mergulho médio de 36°, discordando das medidas do restante da área mapeada. A interseção das lineações indica uma possível dobra pós-evento deformacional principal, caracterizada por um eixo com mergulho para sudeste (Figura 8a). Outra feição observada em campo foi uma região marcada por uma zona de cisalhamento (N-S) sinistral associada a um veio pegmatítico (Figura 8b).

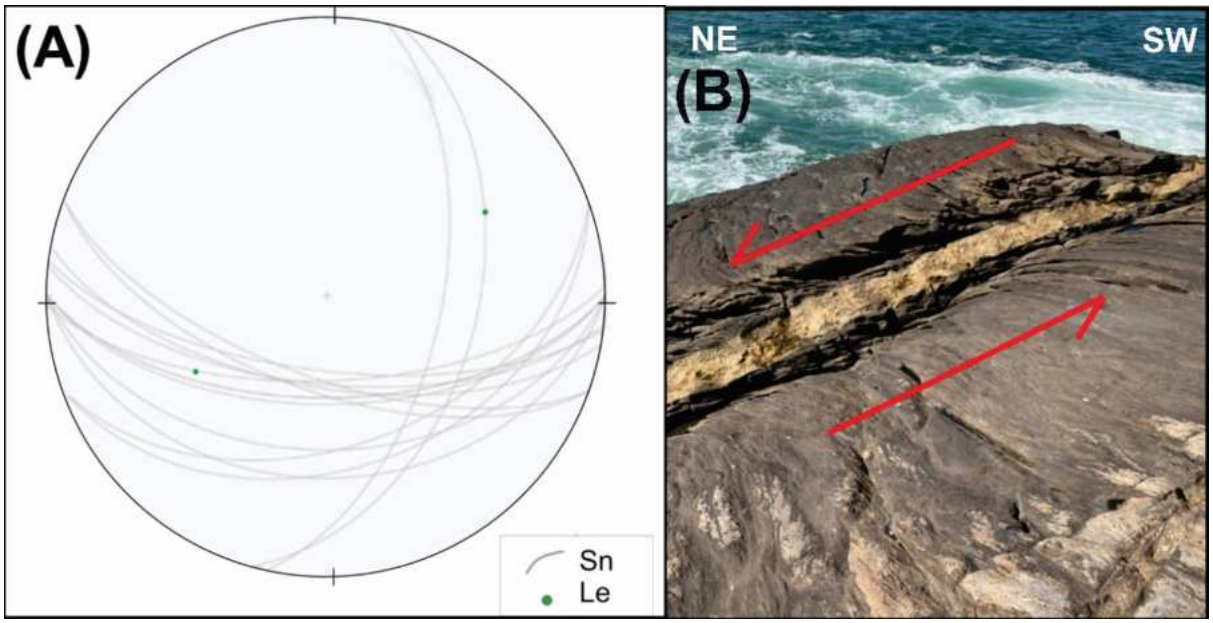

Figura 8 – Feições estruturais na área do Morro Carra de Cão: (A) Estereograma com medidas de foliação tectônica principal (Sn) e lineação de estiramento (Le) das unidades ortognaisse facoidal e cordierita-granada-biotita paragnaisse migmatítico; (B) Fotografia e interpretação gráfica de veio pegmatítico com zona de cisalhamento sinistral.

ii. Avenida Niemeyer

Os litotipos mapeados na Avenida Niemeyer são o quartzito micáceo, o cordierita-granada-biotita paragnaisse migmatítico, o ortognaisse facoidal e diques pegmatíticos (Fig. 4b).

O quartzito caracteriza uma camada homogênea de aproximadamente 50 metros de espessura, de cor clara e com porções mais micáceas escuras. A granulometria é média a grossa e sua mineralogia principal inclui quartzo, feldspato, plagioclásio, biotita e silimanita.

O cordierita-granada-biotita paragnaisse migmatítico aflora ao longo da Avenida Niemeyer (desde a ponta do Mirante do Leblon até a Praia do Vidigal). Possui uma coloração cinza escura, ocasionalmente avermelhada devido ao intemperismo. Apresenta níveis migmatíticos e cristais de tamanho médio a grosso, apresentando granada e cordierita até 4 cm. Localmente apresenta dobras isoclinais, demarcadas por porções quartzosas e micáceas, que acompanham a foliação metamórfica.

O ortognaisse facoidal aflorante na encosta da Avenida Niemeyer, apresenta coloração cinza claro homogênea e granulação fina a média com fenocristais de feldspato de variados tamanhos, alcançando até 15 cm.

Os diques de pegmatito, com espessura aproximada de 30 centímetros, intrudem o paragnaisse. A mineralogia é composta de quartzo, feldspato e biotita.

A análise estrutural da área mostra que o cordierita-granada-biotita paragnaisse migmatítico apresenta foliação metamórfica com direção leste-oeste e baixo mergulho para o sul, de 25 e 35°. A lineação de estiramento (Le) tem caimento para oeste-sudoeste (Figura 9a). O quartzito exibe foliação metamórfica próxima a do paragnaisse, com direção leste-oeste e mergulho para sul.

Os dique pegmatíticos intrudem na direção NW-SE com mergulhos que variam de 55 a 75° para NE. Na proximidade dos diques é possível observar indicadores cinemáticos através do arraste do bandamento metamórfico (Figura 9c). Os diques apresentam-se associados tanto a movimentos dextrais quanto sinistrais (Figura 9b), também foram observados componentes de movimento vertical normal menos expressivos.

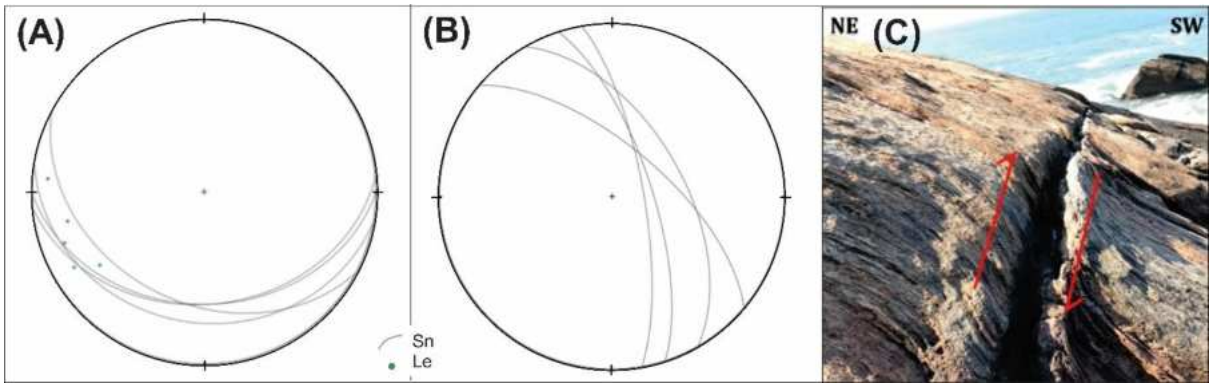

Figura 9 – Feições estruturais na área da Avenida Niemeyer: (A) Estereograma com medidas de foliação tectônica principal (Sn) e lineação de estiramento (Le) da unidade cordierita-granada-biotita paragnaisse migmatítico; (B) Estereograma com medidas Sn de diques pegmatíticos; (C) Fotografia e interpretação gráfica de dique pegmatítico com arraste do bandamento metamórfico dextral normal.

IV. RESULTADOS - artigo científico na íntegra (em inglês)

U-PB AND LU-HF ZIRCON ANALYSIS IN A HOT-OROGEN: ORIENTAL TERRANE, RIO DE JANEIRO (título provisório)

Authors:
Sofia Goldbach d'Orsi[1], Renata da Silva Schmitt[1], Silvia Regina de Medeiros[1], Mauro Cesar Geraldes[2]

Filiations:
[1]Federal University of Rio de Janeiro
[2]Rio de Janeiro State University

Abstract:

During the convergence of the São Francisco and the Congo-Angola paleocontinents, between 600 and 500 Ma, sedimentary basins were generated and their record is preserved in paragneisses. Within the Ribeira Orogen, the Oriental Terrane is mostly constituted by paragneisses intruded by voluminous batholiths pre-, syn- and post-collisional. Here we investigate the origin of the paragneisses that crop out in Rio de Janeiro city (Brazil). The São Fidélis Group consists mostly of cordierite-sillimanite-garnet-biotite paragneisses with minor quartzite layers at granulite facies. Peak metamorphic conditions were 750–800°C below 7 kbar. Our goal is to study the provenance of the protoliths and the basin's tectonic evolution, as this unit underwent high-temperature metamorphism above the zircon closure temperature for the U-Pb system. The methodology combined zircon U-Pb and Lu-Hf analyses. Fieldwork was conducted at Niemeyer Avenue and Morro Cara de Cão. Three samples from distinct lithologies were analysed: cordierite-sillimanite-garnet-biotite paragneiss (kinzigite), fine-grained biotite paragneiss, and micaceous quartzite. Data shows that all lithologies have a similar pattern of distribution for detrital zircon populations. The main Neoproterozoic populations are: 980-930 Ma, 856-838 Ma, 800-740 Ma and 690-580 Ma. The peaks coincide with the ages of the magmatic arcs described in the Oriental Terrane, suggesting them as sources. A younger zircon population seen in the range of 570-550 Ma could be either interpreted as metamorphic or magmatic, due to Pb-loss caused uncertainties. Minor Mesoproterozoic and Paleoproterozoic detrital populations might source from the Kunene Anorthosite Complex and the Eburnean magmatic units of the Angola Craton and the Cabo Frio Tectonic Domain. The Neoproterozoic εHf values for the dated detrital zircons range from +5 to -18, which is feasible with a source from an ancient magmatic arc. The youngest detrital zircon and minimal depositional age for the basin is calculated as 570 Ma, supported by the crystallisation age of the Facoidal Orthogneiss unit, intrusive in the paragneisses. The short interval between metamorphism and deposition on the basin suggests it is a syn-orogenic basin, probably a back-arc or forearc and therefore the metamorphism would be attributed to a regional thermal anomaly related to the hot-orogen.

Key-Words: Detrital zircon, U-Pb geochronology, Lu-Hf geochronology, Oriental Terrane, Ribeira Belt, Hot-orogen.

1- Introduction:

Detrital zircon geochronology is widely used to unravel the tectonic evolution of basins formed in ancient orogenic belts (Kelly and Harley, 2005; Gehrels, 2014; Condie *et al.*, 2017; Barham *et al.*, 2022). However, there is a significant limitation when these orogenic domains have a high geothermal gradient. In these cases, the inferred age of sedimentation using U-Pb and combined Lu-Hf isotopic analyses in detrital zircons is hampered by the overprint of high-temperature metamorphism, that opens the U-Pb system and may lead to Pb-loss, thereby affecting age measurements (Rubatto *et al.*, 2001; Moecher and Samson, 2006; Gehrels, 2011; Tedeschi *et al.*, 2023).

Zircons are highly effective in preserving the age of the sources for sedimentary basins, but at temperatures above 700-750°C, the U-Pb system can reset (Zheng *et al.*, 2005; Harley *et al.*, 2007), making it challenging to interpret the timing of sedimentation and metamorphism. In addition, in tectonically active convergent settings, the fast rate of tectonic processes may bring the ages of sedimentation and metamorphism in the same interval within errors (Cawood *et al.*, 2012; Jian *et al.*, 2022).

Here, we address this problem, trying to overcome the high-temperature influence of the metamorphism by using this and other geological evidence to infer the age of the source rocks of the basin and its tectonic evolution from sedimentation to metamorphism. In this study, three samples from the paragneisses of Rio de Janeiro city, within the Oriental Terrane - a hot orogenic domain of the Ribeira belt in SE Brazil (Bento dos Santos *et al.,* 2015; Valeriano *et al.,* 2016) - were studied to evaluate the use of U-Pb geochronology and combined Lu-Hf methodologies for a more comprehensive understanding of the age and origin of the sedimentary basin that served as the protolith of these HT-LP gneisses.

2 - Geological setting:

2.1 - Ribeira Belt, Oriental Terrane:

The Ribeira belt originated during many stages contained in the convergence of the São Francisco and the Congo-Angola paleocontinents during the Neoproterozoic and the Cambrian. This orogen extends along the southeastern margin of Brazil, extending north as the Araçuaí Orogen and southwest as the Luis Alves Craton (Fig. 1a). The central Ribeira Orogen segment is composed of four tectonic domains from NW to SE: Occidental Terrane, Paraíba do Sul-Embu Terrane, Oriental Terrane and Cabo Frio Tectonic Domain (Fig. 1b) (Heilbron *et al*., 2008; Trouw *et al*., 2013).

This work investigates the Oriental Terrane, which crops out in Rio de Janeiro city (Brazil), and integrates some worldly known landscape (eg. Christ the Redeemer, Copacabana beach). This unit is mostly constituted by paragneisses (Costeiro Domain) together with pre-, syn- and post-collisional igneous intrusions considered magmatic arcs. Para-derived rocks of this terrane form the São Fidélis Group (Valeriano *et al*., 2012) and consist mostly of cordierite-sillimanite-garnet-biotite gneisses with minor quartzite layers. This group can be subdivided in Upper São Fidélis (top) and Lower São Fidélis (basal), which are respectively characterised predominantly as kinzigitic gneiss and as sillimanite biotite gneiss (Kühn *et al*., 2004; Tupinambá *et al*., 2012; Heilbron *et al*., 2020).

Magmatic arcs of the Oriental Terrane are the Rio Negro arc, the Serra da Prata arc and the Serra da Bolívia arc (Peixoto *et al*., 2017), as well as younger syn-, late- and post-orogenic magmatic units. The Serra da Prata Complex crops out in the north-northeast region of Rio de Janeiro State (Heilbron *et al*., 2020). It registers granitoid crystallisation ages from 856-838 Ma (Peixoto *et al*., 2017). The Rio Negro Arc represent pre-orogenic meta-igneous units date from 630-595 Ma (Heilbron and Machado, 2003; Tupinambá *et al*., 2003). This complex originated as a magmatic arc that developed into a primitive intra-oceanic setting and then became a cordilleran arc (Tupinambá *et al*., 2012). The Serra da Bolívia Arc formed around 595-570 Ma Ma as a cordilleran magmatic arc. It extends north into the Rio Doce arc of the Araçuaí belt and south into the Socorro arc (Hackpacher *et al*., 2003; Heilbron *et al*., 2013). The two Ediacaran-Cambrian magmatic events are correlated to the 570-540 Ma Facoidal Orthogneiss unit and the 510-480 Ma post-collisional magmatic intrusions (Valeriano *et al.,* 2011; Martins *et al*., 2022).

The mineral association biotite + cordierite + garnet + plagioclase + k-feldspar + quartz (+ liquid) records granulite facies and peak metamorphic conditions of 750–800°C and ca. 7 kbar, implying a geothermal gradient of about 40°C/km (Kühn *et al*., 2004).

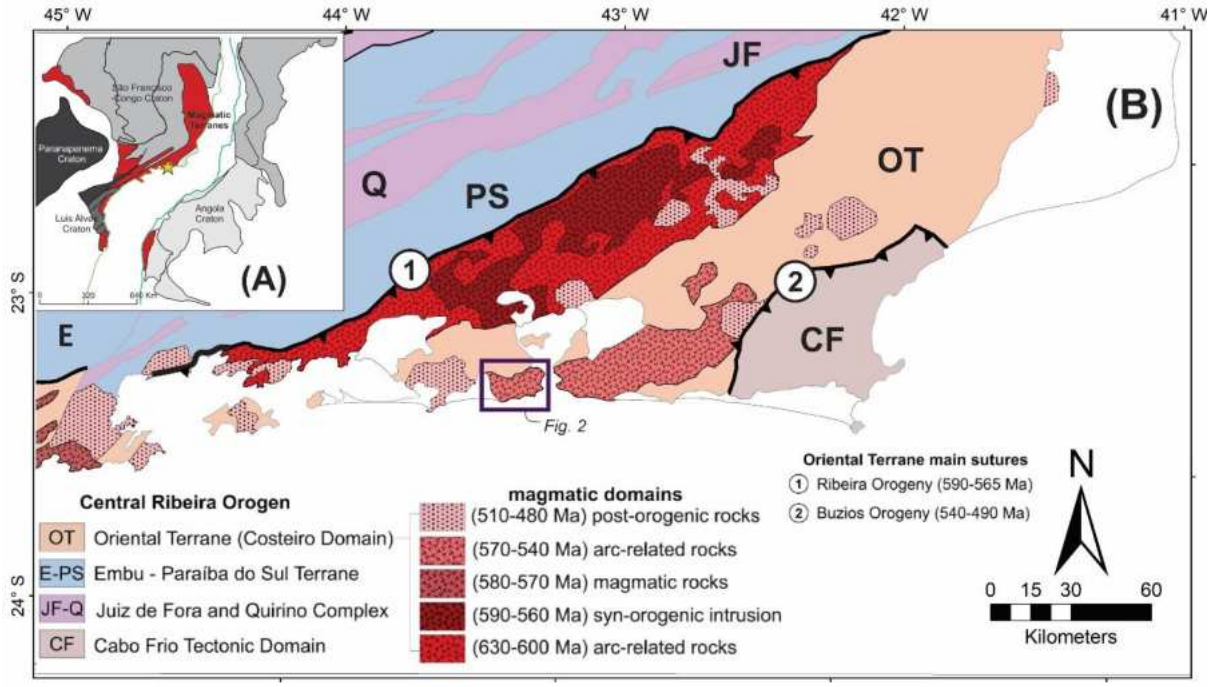

Figure 1 - (A) South America and Africa reconstructed as Gondwana, modified from Vieira et al. (2022). (B) Tectonic map of the Central Ribeira Orogen with magmatic domains in the Oriental Terrane (modified from Martins et al., 2022).

2.2 - Zircon Provenance in São Fidélis Group

Previous provenance studies on Costeiro Domain's sedimentary rocks of São Fidélis Group were made by Valladares *et al.* (2008), Fernandes *et al.* (2015), Lobato *et al.* (2015), Peixoto *et al.* (2022) and Freitas *et al.* (2024) on different locations. Zircon ages are Paleoproteroic, Mesoproterozoic and Neoproterozoic. Neoproterozoic data point to multimodal sources, correlated to Serra da Prata Arc and Rio Negro Arc. There is record of Angola craton sedimentary contribution.

Previous provenance studies on the metasedimentary sequences from Búzios and Palmital successions (Schmitt *et al.*, 2004; Fernandes *et al.,* 2015; Freitas *et al.*, 2024), related to the Cabo Frio Terrane, ha been compiled as units adjacent to the Costeiro Domain. Búzios succession show a principal Neoproterozoic source and a less expressive Mesoproterozoic source. Palmital succession show a main source from the Neoproterozoic and minor Mesoproterozoic and Paleoproterozoic sources.

3 - Methodology:

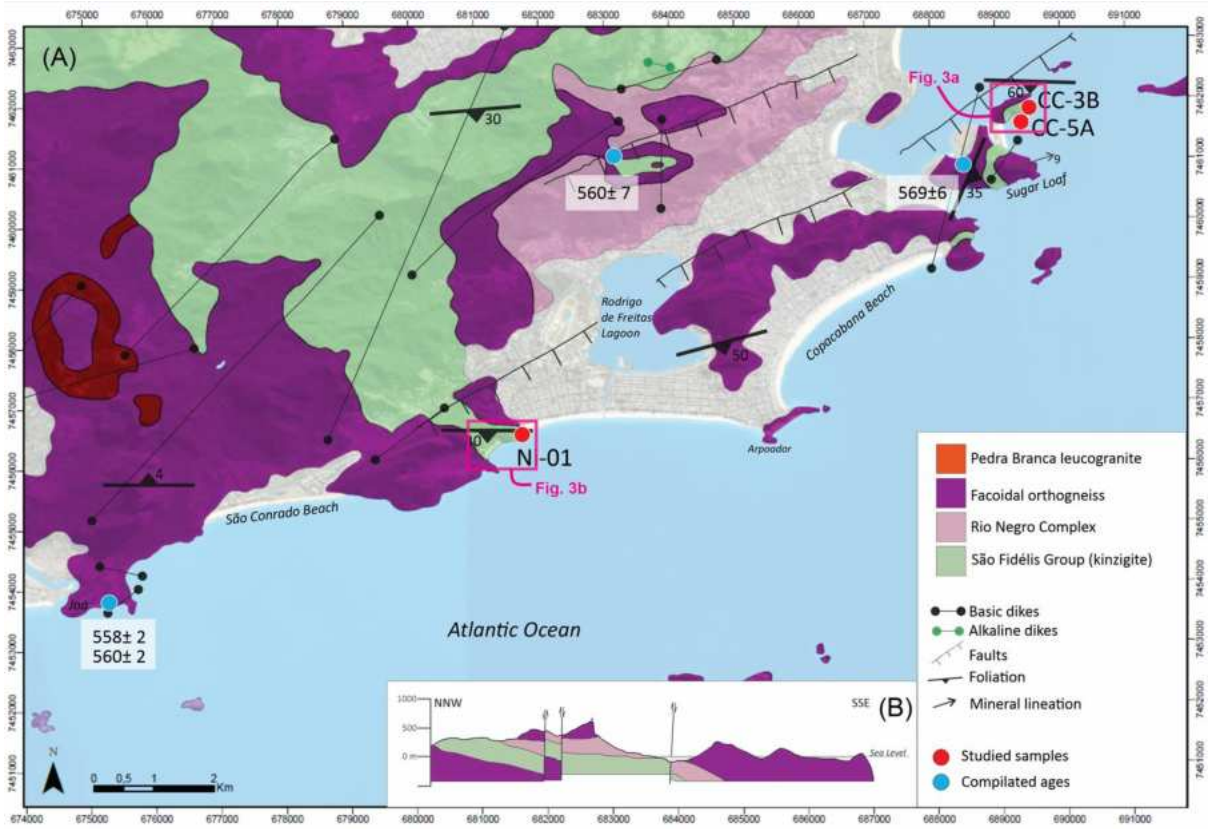

Figure 2 – (A) Geological map of Rio de Janeiro region modified from Heilbron et al. (2020) and Valeriano et al. (2012). U-Pb crystallisation ages compiled from Martins et al. (2022) and Silva et al. (2003). (B) Schematic geological cross-section modified from Valeriano et al. (2000).

3.1 - Sampling and sample preparation:

To provide context for the geological samples, detailed maps at a scale of 1:5000 were made for Morro Cara de Cão (Urca) and Niemeyer Avenue (Vidigal) areas (Fig. 2). At Morro Cara de Cão, 6 samples were collected, with two for geochronology; at Niemeyer Avenue, 5 samples were collected, with 1 for geochronology. The remaining samples were used for thin-section description.

Field data, including petrographic and structural analysis resulted in a geological map and a cross-section for each area. The maps and sections were created using ArcMap 10.5 and CorelDraw 2020 softwares. Thin sections were described using a Zeiss petrographic microscope Axioskop 40. The provenance study involving detrital zircon analysis utilised three samples, each from a distinct lithology. Sampling was conducted during two fieldwork campaigns at two distinct locations: Morro Cara de Cão and Niemeyer's coastline (Rio de Janeiro). During the sample collection, potential pegmatite veins associated with the target rock were avoided. The collected rock was unweathered.

Samples were mainly processed in LAG (Geology Department) at the Federal University of Rio de Janeiro (UFRJ). For each sample, zircon grains were separated from 8-12 kg of crushed rocks by using heavy liquid combined with magnetic techniques such as: jaw crusher, disk grinder, manual panning, Frantz isodynamic magnetic separator, density separation (bromoform and methylene iodide) and ultrasonic bath. Around 200-250 zircon grains from each sample were selected from other dense and diamagnetic minerals (mainly rutile) to make an epoxy resin mount to be analysed. No handpicking, visual morphological or colour differentiation was done. Therefore, assuring that the distribution of zircons analysed in laboratories mirrors the real detrital age of the para-sediments without any bias (Andersen, 2005).

Transmitted light (TL) and cathodoluminescence (CL) images were obtained to better understand the grain's morphological characteristics (McLaren *et al.*, 1994). Those images were considered during the laser spot's selection for all grains.

3.2 - U-Th-Pb isotopic analyses

The U–Pb analyses were conducted using LA-ICP-MS at MULTILAB-UERJ, utilising the Neptune plus (laser ablation inductive coupled plasma multi-collector mass spectrometry). Operating conditions of LA-ICP-MC-MS in the U-Pb method were used according to Geraldes *et al.* (2015). Ablation was performed with a spot size of 40 micrometres, at a frequency of 6 Hz, and an intensity of 8 mJ. The material ablated was transported by a flow of helium (0.5 L/min) during the analysis, consisting of 50 cycles of 1 second each. The calibration was made using reference zircon material.

It was defined by Vermeesch (2004) that at least 117 grains per sample have to be dated in order to avoid bias. In this study, 120 U-Pb age measurements were conducted for each of the three samples.

The data collected was later processed using ISOPLOT 3.0 (Ludwig, 2003). The software was used to calculate $^{207}Pb/^{235}U$, $^{206}Pb/^{238}U$, and $^{207}Pb/^{206}Pb$ ages and generate Concordia Tera and Wasserburg (1972) diagrams. Throughout this work, interpretations used $^{207}Pb/^{206}Pb$ ratio for grains older than 1.2 Ga and $^{206}Pb/^{238}U$ ratios for grains younger than 1.2 Ga. A margin of 10% discordance was implemented for provenance analysis.

3.3 - Lu-Hf isotopic analyses

Lu-Hf measurements were performed on 60 detrital zircon grains previously dated through U-Pb LA-ICP-MS. Thirty grains were selected from samples CC-05A (cordierite-

sillimanite-garnet-biotite gneiss) and CC-03B (biotite gneiss) aiming on an unbiased age distribution while limited by the grain's size. The procedure was conducted using LA-ICP-MS at MULTILAB-UERJ, utilising Neptune Plus (Thermo Scientific). Instrument specifications for Lu-Hf followed the parameter from Geraldes *et al.* (2015), spot size is 40 micrometres and frequency is 10 Hz. Calibrations utilised standards GJ-01, 91500 and MudTank.

The decay constant value for ^{176}Lu was 1,876 x 10^{-11}/year (Söderlund *et al.*, 2004). The depleted mantle (DM) model in reference to present-day uses the values 0.28325 for $^{176}Hf/^{177}Hf$ and 0.0388 for $^{176}Hf/^{177}Hf$ (Griffin *et al.*, 2000; Andersen *et al.*, 2009). Lu–Hf chondritic (CHUR) parameters are $^{176}Lu/^{177}Hf$=0.0336±1 and $^{176}Hf/^{177}Hf$=0.282785±11 (Bouvier *et al.*, 2008).

4 – Results:

4.1. Geology of the area:

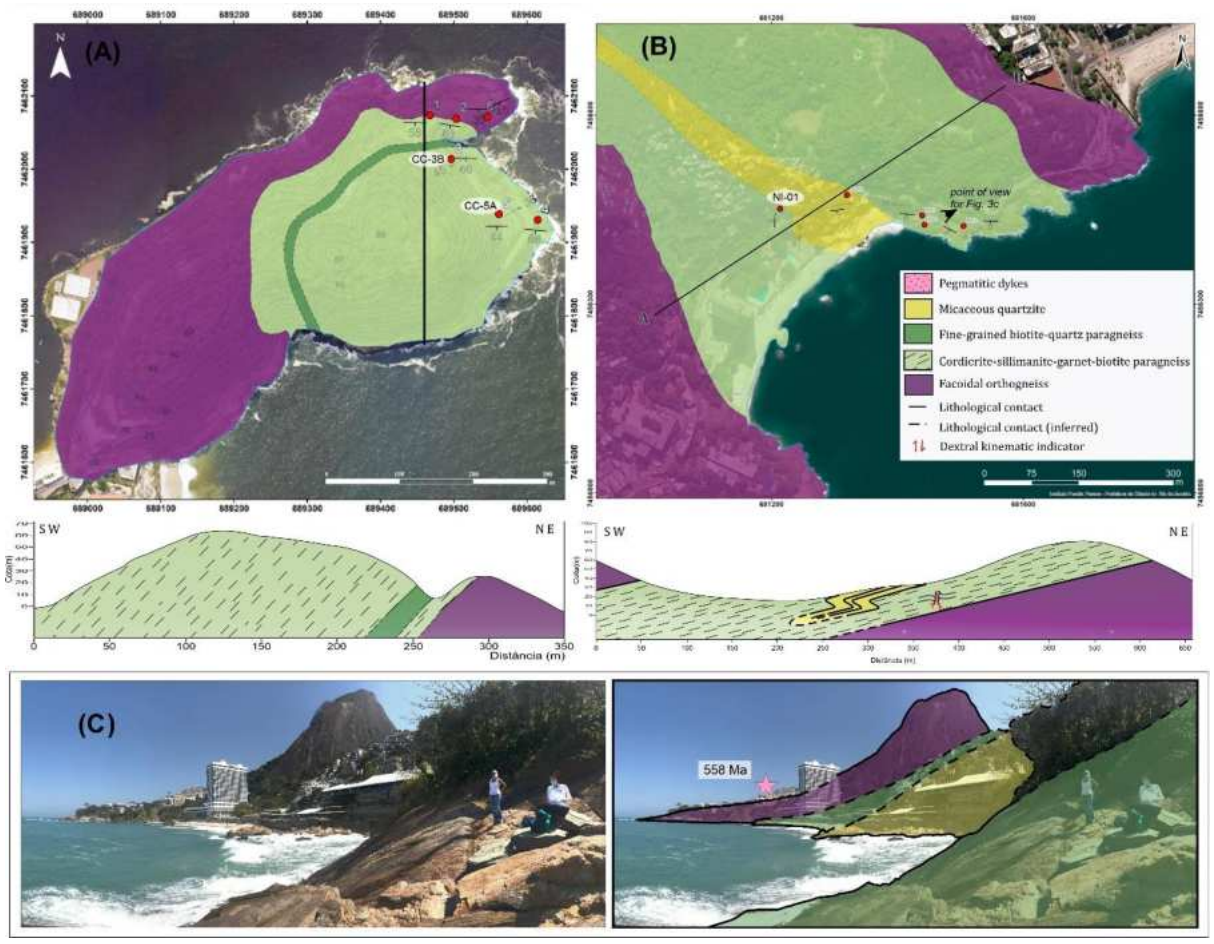

*Figure 3 – Geological map and cross-section of the studied areas in Rio de Janeiro city: (A) Morro Cara de Cão (Urca) and (B) Niemeyer Avenue (Vidigal). (C) Field photography and overlapped geological interpretation. Colour interpretation follows caption used in previous figure. Photo taken toward SW from shore next to Leblon Belvedere (Niemeyer Avenue). Star marks approximate sample location for 558 ± 2 Ma Facoidal orthogneiss (*Martins *et al.*, 2022*) in relation to the studied outcrop.*

In both Morro Cara de Cão (Fig. 3a) and Niemeyer Avenue (Fig. 3b) areas, there are two main mapping units, which are interleaved: an orthogneiss unit (Fig. 4a) and a paragneiss unit (Fig. 4d). In the traditional geological bibliography of Rio de Janeiro, the paragneiss is known as “kinzigite” and the orthogneiss as “Facoidal” or “Augen-gneiss”. The main foliation is parallel to the lithological contacts, indicating that both units were deformed together.

At the Cara the Cão area, gneissic foliation dips in a low to moderate angle to the south, with the paragneiss unit covering the orthogneiss. Intrafolial folds occur in the paragneiss (Fig. 4e). Foliation is marked mainly by planar orientation of biotite in both units, and also by the orientation of feldspar megacrystals (mainly of K-feldspar) in the orthogneiss. Thin lenses of a fine-grained dark grey paragneiss occur in the migmatitic paragneiss (Fig. 4h). Stretching lineation and quartz megacrystal mineral lineation dip towards the south and southeast.

Along the Niemeyer Avenue prevail paragneiss kinzigite exhibiting stromatic migmatitic texture (Fig. 4g). Gneissic banding dips in low angle (25 to 35°) to the south and locally present intrafolial folds. In this outcrop, paragneiss is beside Augen orthogneiss and micaceous quartzite. A quartzite layer was identified as approximately 50 m thick (Fig. 4c). The quartzite has a light pinkish colour and is coarse grained with mica (Fig. 4b). It is in gradual contact with the kinzigite. Metamorphic foliation of the quartzite is similar to the paragneiss, dipping south.

In both areas, pegmatitic dikes of 1 to 2 metre thick with compositional change (Fig. 4j) from border to centre arranged in northwest-southeast structures point to sinistral kinematics marked by a drag of the main tectonic foliation (Fig. 4i).

Field data, together with reference studies in those areas (eg. Valeriano and Magalhães, 1984), show that the Augen orthogneiss unit intrudes the paragneiss. There is an absence of older deformation structures, such as the mentioned intrafolial folds, in the orthogneiss. In other locations in Rio de Janeiro (eg. Joatinga beach at Joá, next to Barra da Tijuca neighbourhood), xenoliths of paragneisses inside orthogneiss reinforce this relation. Field data suggest intercalation between quartzite and paragneiss, with layers folding into isoclinal folds (Fig. 3b; Fig. 3c).

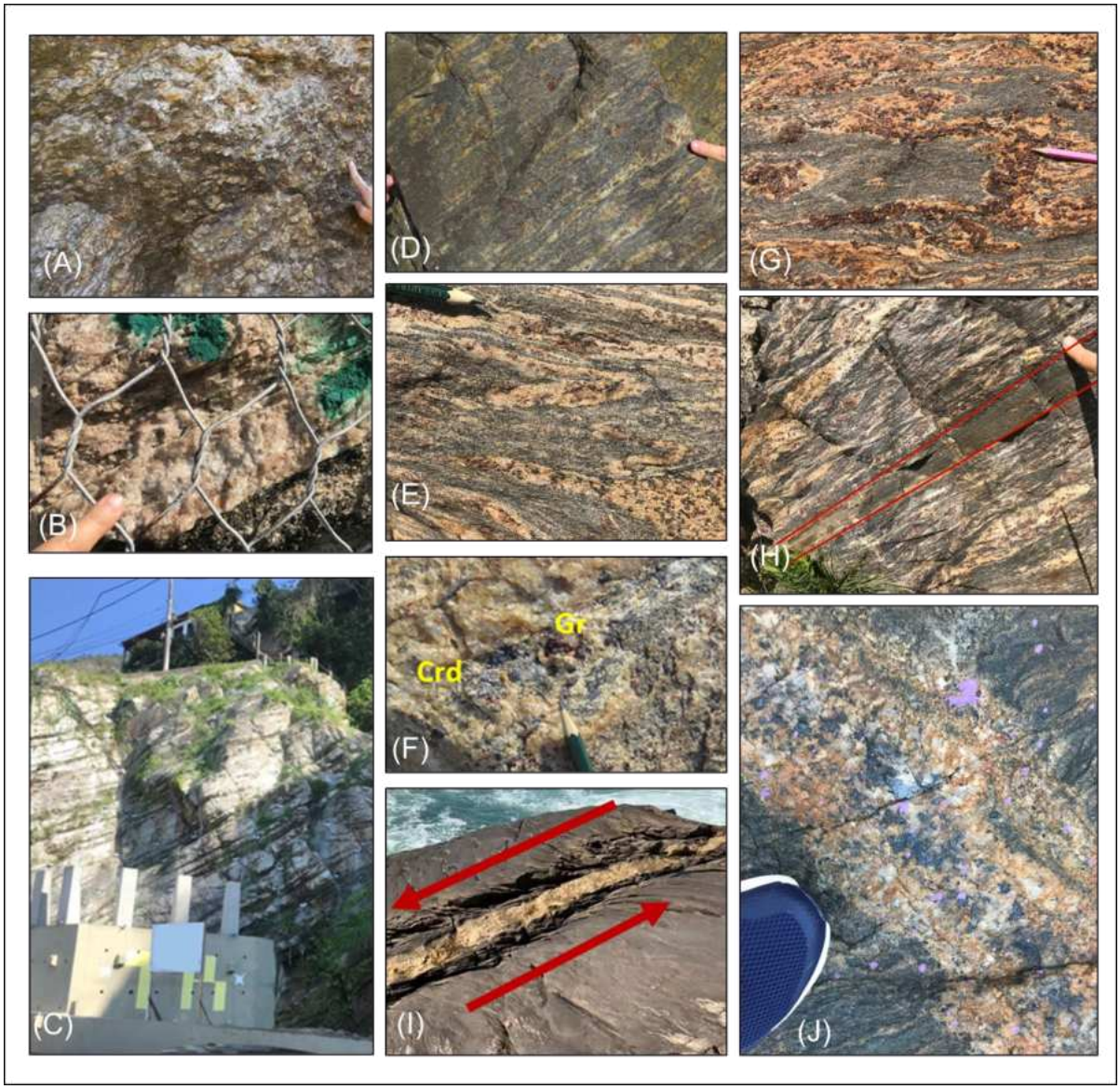

Figure 4 - Field photography of identified lithologies and geological features. (A) Facoidal orthogneiss. (B) and (C) Quartzite. (D) Paragneiss with (E) isoclinal fold, (F) Gr-garnet and Crd-cordierite and (G) stromatic texture and garnet porphyroblasts. (H) Fine biotite gneiss layer in paragneiss with melano- and leucosome. Pegmatite recording (I) sinistral shear sense from related drag folds and (J) compositional change. A, B, C, E, F and J at Niemeyer Avenue area; D, G, H and I at Morro Cara de Cão.

4.2 - Para-derived lithotypes

In both areas, three lithologies were identified as products of metamorphism of sedimentary rocks. The main aspect used to define this kind of protolith was the presence of sillimanite and garnet as well as gneissic banding inherited from preexisting primary foliation. The lithotypes were separated in cordierite-sillimanite-garnet-biotite gneiss, biotite gneiss and quartzite, and the geochronology sample identification for each of them were CC-05A, CC-03B and Ni-01, respectively. The sample collection sites are shown on the geological map (Fig. 3a; Fig. 3b; Table 1).

Sample	Location	Coord_X	Coord_Y	Lithotype	Number of zircon grains U-Pb	Number of spots U-Pb	Number of spots Lu-Hf
CC_05A	Morro Cara de Cão	689562	7461939	Cordierite-sillimanite-garnet-biotite gneiss	79	88	30
CC_03B	Morro Cara de Cão	689497	7462014	Fine-grained biotite gneiss	45	48	30
Ni_01	Niemeyer Av.	681225	7456402	Quartzite	86	86	-

Table 1 - Samples selected for isotopic geology. (Number of analyses within concordance criteria).

4.2.1 Cordierite-sillimanite-garnet-biotite gneiss:

Cordierite-sillimanite-garnet-biotite gneisses from Rio de Janeiro were also described in literature as kinzigites (Kühn *et al.*, 2004). The rock presents widespread stromatic migmatization. It exhibits garnet and cordierite porphyroblasts of up to 3 cm (Fig. 4f) restricted to the leucosome. The presence of intrafolial folds was constantly observed as a reflection of the structure of the area.

The gneiss has medium to coarse grain size and is composed of quartz, biotite, garnet, plagioclase (An10), cordierite, and sillimanite, in addition to opaque minerals and accessory or trace minerals such as titanite and monazite. Furthermore, sub-millimetre-sized zircon grains are included in garnet and biotite.

Garnet is one of the most abundant minerals, appearing as millimetre to centimetre poikiloblastic crystals with inclusions of biotite, plagioclase, and quartz (Fig. 5c). Biotite is reddish possibly due to high Ti composition (Fig. 5b). Quartz appears as polygonal or anhedral crystals with undulatory extinction (Fig. 5a). Cordierite may contain zircon and titanite inclusions and secondary chlorite (Fig. 5g). Sillimanite occurs in up to 1 mm crystals (Fig. 5d).

Those characteristics and mineral paragenesis assembly indicate metamorphism on high-temperature medium-pressure granulite facies.

4.2.2 - Biotite gneiss:

The biotite gneiss unit was identified only at Morro Cara de Cão in a 30 cm thick lens near the contact zone between the augen-orthogneiss and the cordierite-sillimanite-garnet-biotite gneisses. The rock did not show any sign of partial melting.

This gneiss is dark grey and presents fine to very fine texture. It has quartz, plagioclase, garnet, biotite, zircon, and opaque minerals. Quartz composes the recrystallized matrix with granoblastic texture and grain size 0,2 mm (Fig. 5f). Poikiloblastic garnet displayed includes quartz, plagioclase, and biotite. Biotite often shows chlorite as a substitutive mineral (Fig. 5g). Zircon appears both in the matrix and included in garnet.

The high percentage of quartz could suggest a psammitic protolith.

4.2.3 – Quartzite:

The quartzite constitutes a 10 metres thick body intercalated in the paragneiss. It locally presents a composition layering of light grey/white purer quartzite and biotite-rich darker quartzite. Intercalated layers vary from millimetric to maximum 5 cm. The quartz displays significant metamorphic recrystallization.

Analysed samples contain quartz, K-feldspar, microcline, biotite, sillimanite, garnet, opaque minerals, and traces of rutile (Fig. 5h). Biotite is notably abundant reaching ca. 10-15% of the samples (Fig. 5i). Sillimanite is extensively observed oriented and included on recrystallized quartz that composes the matrix.

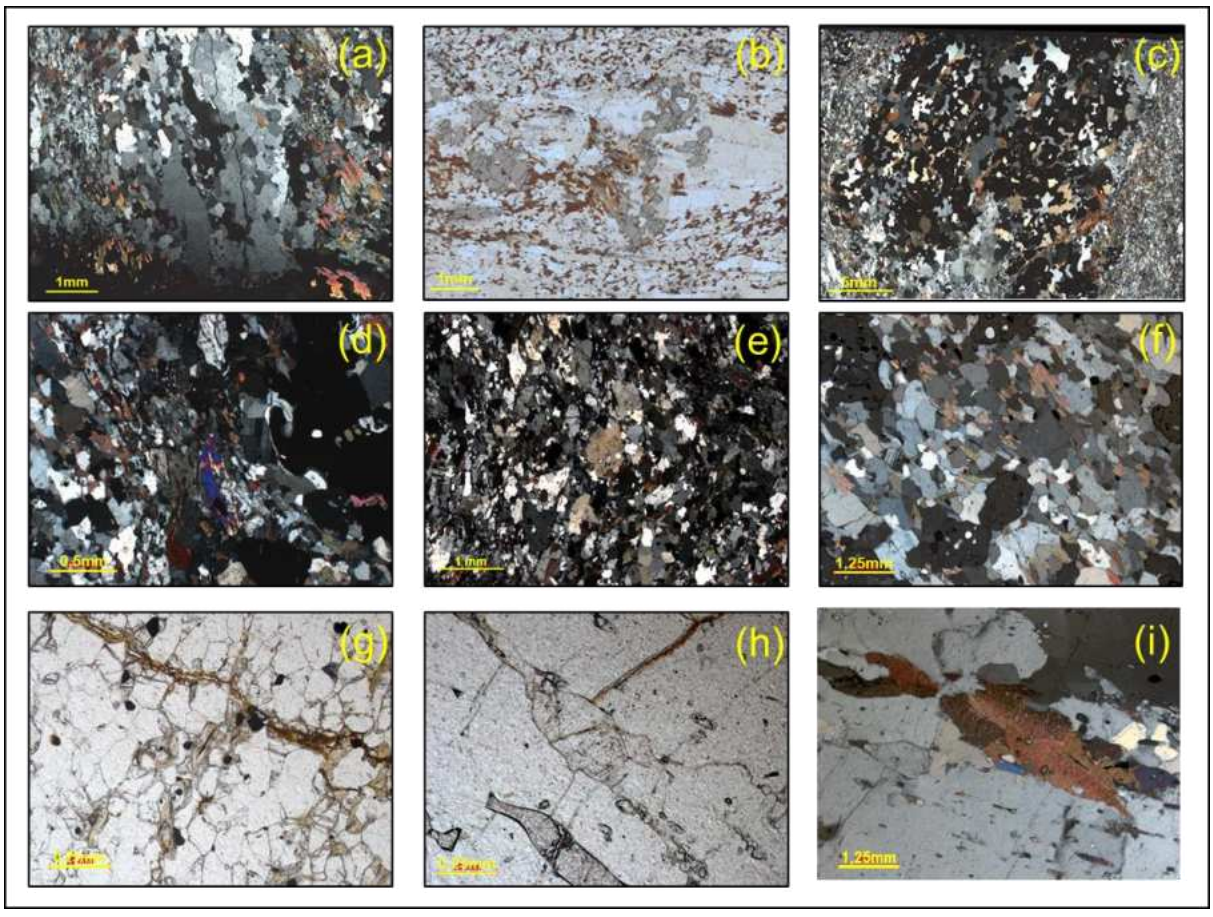

Figure 5 - Photomicrographs of the lithotypes (taken with AxioCam Mrc): Cordierite-sillimanite-garnet-biotite paragneisses with (a) recrystallized quartz crystals with polygonal contacts, (b) Ti-rich biotite defining foliation, (c) centimetric poikiloblastic garnet, (d) sillimanite, (e) poikiloblastic cordierite. Fine-grained biotite gneiss: (f) quartz polygonal contacts and oriented biotite, (g) chloritized biotite. Micaceous quartzite: (h) K-feldspar and garnet crystals, (i) biotite as the main mica.

4.3 - U-Th-Pb zircon data

This study obtained a total of 233 concordant age analyses on zircon cores from 3 paragneiss samples, in order to obtain provenance ages. Because most of the zircon crystals

show thin metamorphic rims (less than 40 µm of overgrowth), only 12 crystals were able to be analysed twice: both the core and rim.

The youngest zircon crystals from all samples, especially from the two paragneisses, present a random mix of typical metamorphic and typical detrital morphology (Fig. 7d; Fig. 8d; Fig. 9d). Those grains were subjected to detailed analysis to determine the deposition limit for the basin. Zircons interpreted as metamorphic are rounded and show sector zoning (Rubato, 2017). Zircon interpreted as detrital present typical concentric growth zones and central cores surrounded by more recent growth rims (Corfu *et al.*, 2003; Hoskin and Schaltegger, 2003). Unfortunately, we were unable to point a clear geochronological boundary between detrital and metamorphic zircons using only the morphological analysis.

Additionally, in an attempt to isolate the metamorphic fraction from the data, the Th/U ratio of the three samples was studied. Metamorphic zircon domains tend to have lower Th/U values; however, the dispersion of our data does not reflect this pattern (Fig. 6) and could not be used to help provide a definitive age limit for the metamorphism. This Th/U signature can be justified by the presence of monazite and/or garnet in high-temperature metamorphism (Williams e Claesson, 1987; Pidgeon, 1992; Schaltegger *et al.*, 1999). In light of these data, interpretations of detrital and metamorphic zircon will be approached in the discussion, relying on regional geology as a reference framework.

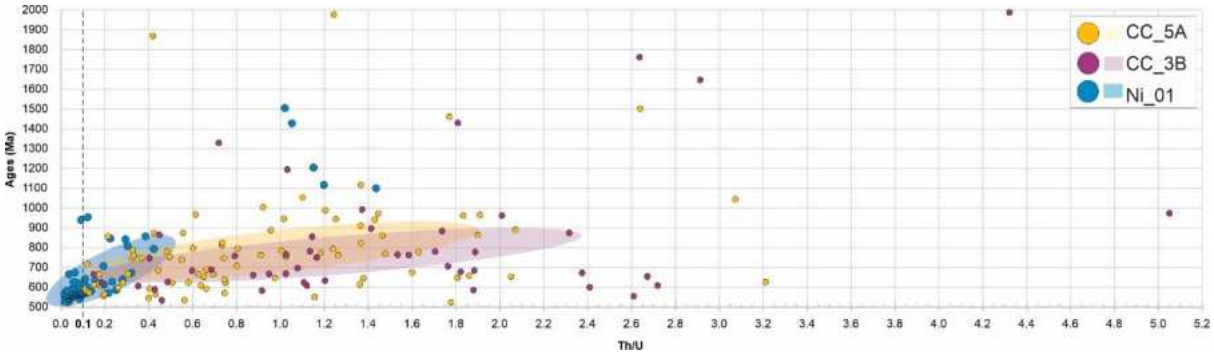

Figure 6 - Th/U ratios versus Age (Ma) to discriminate between metamorphic (Th/U<0.10) and magmatic domains of origin (Zheng et al., 2005). Colour ellipses reflect main range distributions from each of the 3 samples.

4.3.1 – Sample CC-05A (Cordierite-sillimanite-garnet-biotite gneiss – Cara de Cão area):

We obtained 88 ages for this sample within the concordant range (10%) (Fig. 7a). The youngest zircon is 523 ± 17 Ma (CC_5A_III_36) and the oldest 1977 ± 41 Ma (CC_5A_III_13). The probability density plot (Fig. 7b) shows a major Neoproterozoic-Cambrian peak (80 spots) and two other minor peaks: Mesoproterozoic, with 6 spots, and Paleoproterozoic, with 2 spots. The Mesoproterozoic zircon ages are: 1003 ± 22 Ma (CC_5A_II_06), 1044 ± 23 Ma (CC_5A_II_37), 1052 ± 23 (CC_5A_III_20), 1117 ± 62 Ma (CC_5A_III_52), 1461 ± 65 Ma

(CC_5A_II_10) and 1502 ± 251 Ma (CC_5A_II_41) .The Paleoproterozoic ages are 1869 ± 68 (CC_5A_II_10) and 1977 ± 41 Ma (CC_5A_III_13).

The majority of the spots are Neoproterozoic (Fig. 7c). The Tonian period shows three age peaks: 990-920 Ma (8 spots), 880-840 Ma (5 spots) and 800-730 Ma (18 spots). The Cryogenian has only one main peak 638-688 Ma zircons. Measures plotting in the Ediacaran (24 spots) and in the Cambrian (2 spots) periods will be later divided as metamorphic and detrital, but, as a general result, there are three age groups: 625-609 Ma (11 spots), 597-583 Ma (5 spots) and 572-544 Ma (8 spots).The age range of 625 to 490 Ma present Th/U ratios scattered between 3.21 and 0.10 (Fig. 6).

In an attempt to separate Brasiliano metamorphic zircons and detrital zircons, we were able to perform two U-Pb spot measurements on 9 crystals - one on the core and one on the rim. The results were not satisfying, although concordant. Only one grain shows a core of 622 ± 39 Ma (CC_5A_II_50) and a rim age of 555 ± 59 Ma (CC_5A_II_51), coherent with the Ediacaran-Cambrian metamorphic age of the belt. This metamorphic rim has a Th/U of 0.19. Within the error, the metamorphic event that affected this sample would be 625-490 Ma.

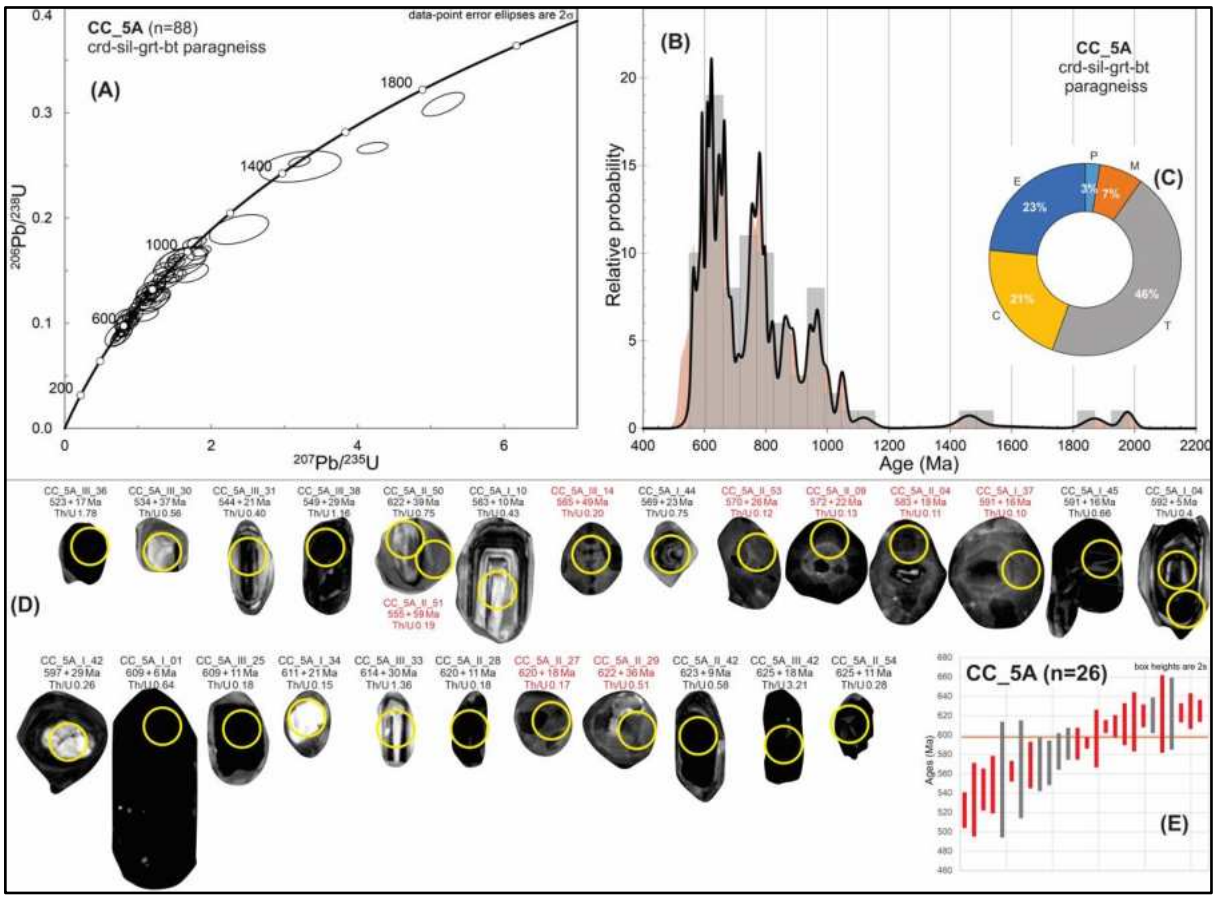

Figure 7 - Sample CC_5A (cordierite-sillimanite-garnet-biotite gneiss). (A) Concordia diagram. (B) Relative age probability/histogram where shaded red area reflects the histogram for all data, while the full black line together with the grey columns represents solely zircons interpreted as detrital (refer to discussion topic 5.1). (C) Sector diagram with detrital zircon distribution (P=Paleoproterozoic; M=Mesoproterozoic; T=Tonian; C=Cryogenian;

E=Ediacaran). (D) Selected cathodoluminescence images of zircon grains between 490 and 625 Ma (yellow circles mark analysed spots for U-Pb). (E) Age distribution in error bars graph. Colour reflects morphological interpretation: black/grey=detrital and red=metamorphic.

4.3.2 – Sample CC-03B (Biotite gneiss – Cara de Cão area):

A total of 48 ages were obtained for the fine-grained biotite paragneiss sample within the concordant range (10%) (Fig. 8a). The youngest zircon is 533 ± 38 Ma (8_CC-3B) and the oldest 2019 ± 53 Ma (148_CC-3B). Probability density plot data (Fig. 8b) reveal the majority of zircon ages fall within the Neoproterozoic-Cambrian period with 42 spots, along with two minor peaks in the Mesoproterozoic and Paleoproterozoic eras, containing 3 and 3 spots respectively.

The Mesoproterozoic zircon ages identified are 1193 ± 34 Ma (61_CC-3B), 1328 ± 146 Ma (46_CC-3B) and 1429 ± 184 Ma (9_CC-3B). The Paleoproterozoic records are two Statherian ages: 1646 ± 207 Ma (59_CC-3B) and 1761 ± 150 Ma (45_CC-3B); and one Orosirian age: 2019 ± 53 Ma (148_CC-3B).

Most zircon ages concentrate in the Neoproterozoic era (Fig. 8c). Two results are from the late Cambrian (533 ± 39 Ma and 554 ± 16). During the Tonian, crystals are distributed in three distinct age peaks: 991-960 Ma (3 spots), 895-854 Ma (5 spots), 781-746 Ma (9 spots). The primary peak spans from 706 to 582 Ma (23 spots), however, it is important to note that these will later be classified as either metamorphic or detrital (Fig. 8d). The age range of 625 to 490 Ma zircons in sample CC-03B reveals Th/U ratios that vary between 2.72 and 0.18.

To further differentiate Brasiliano metamorphic zircons from detrital zircons, we conducted two U-Pb spot measurements on 3 crystals from this lithology, focusing on differentiating the core and the rim. However, the results suggest that chosen spots are from a same zircon crystal domain, not revealing any age consistent with known metamorphism of the Ribeira belt.

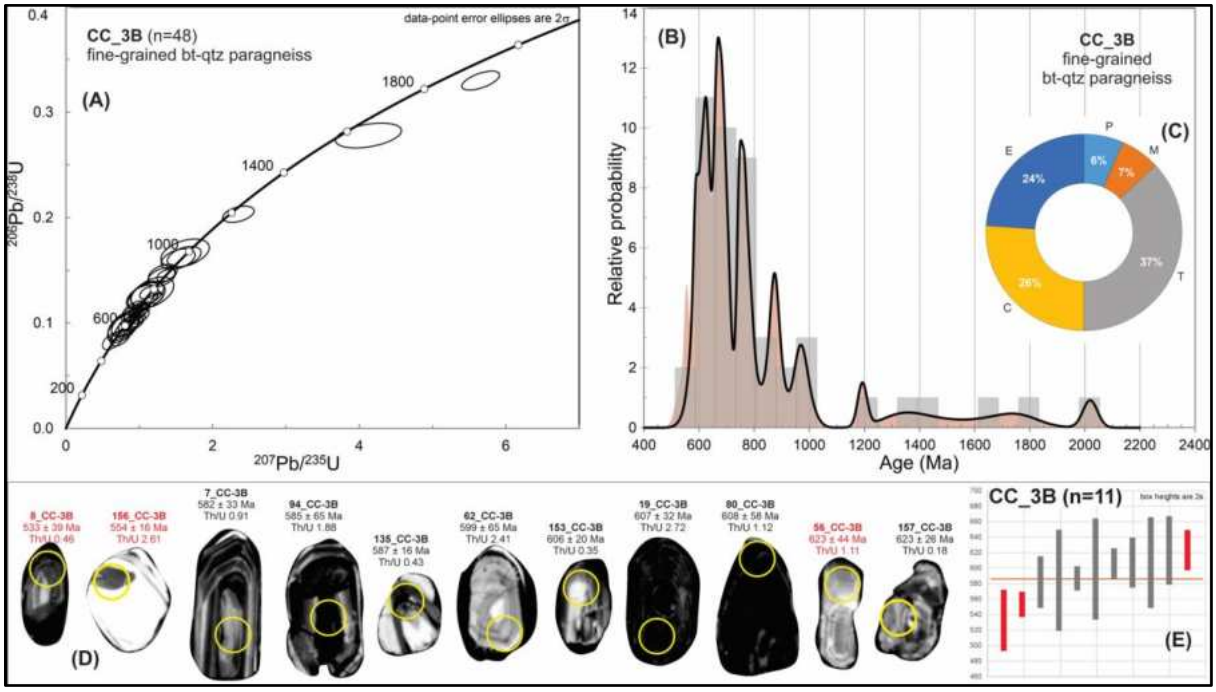

Figure 8 - Sample CC_3B (fine-grained biotite paragneiss). (A) Concordia diagram. (B) Relative age probability/histogram where shaded red area reflects the histogram for all data, while the full black line together with the grey columns represents solely zircons interpreted as detrital (refer to discussion topic 5.1). (C) Sector diagram with detrital zircon distribution (P=Paleoproterozoic; M=Mesoproterozoic; T=Tonian; C=Cryogenian; E=Ediacaran). (D) Selected cathodoluminescence images of zircon grains between 490 and 625 Ma (yellow circles mark analysed spots for U-Pb). (E) Age distribution in error bars graph. Colour reflects morphological interpretation: black/grey=detrital and red=metamorphic.

4.3.3 – Sample Ni-01 (Quartzite - Niemeyer area):

A total of 86 ages were obtained from the quartzite sample within a concordance range of 10% (Fig. 9a). The youngest zircon age is 526 ± 12 Ma (NI_01_042), while the oldest is 1505 ± 78 Ma (NI_01_111). Probability density plot (Fig. 9b) indicates that the majority of zircon ages are concentrated in the Neoproterozoic-Cambrian period, with 81 spots (Fig. 9c).

In the Mesoproterozoic era, there are 5 spot ages: 1100 ± 25 Ma (NI_01_043), 1117 ± 36 Ma (NI_01_092), 1205 ± 79 Ma (NI_01_044), 1428 ± 76 Ma (NI_01_035) and 1505 ± 78 Ma (NI_01_111). These ages are arranged in two smaller peaks in the Calymmian and one in the Late Ectasian-Stenian.

Peak distribution in the Neoproterozoic era had three minor peaks in the Tonian period, one minor peak in the Cryogenian and one main peak mostly in the Ediacaran. Tonian peaks are 954-940 Ma (2 spots), 859-842 Ma (3 spots) and 809-794 Ma (2 spots). Cryogenian peak is 708-666 Ma (4 spots). The main peak ranges from 648 to 526 Ma (70 spots). These younger zircons were categorised as either metamorphic or detrital in an in-depth analysis (Fig. 9d; Fig. 9e). In sample NI-01, zircons aged between 625 and 490 Ma exhibit Th/U ratios ranging from

0.25 to 0.02 (Fig. 6), showing an average value much lower compared to the paragneisses samples.

Particularly for this quartzite sample, the average crystal size was smaller, making morphological analysis more challenging.

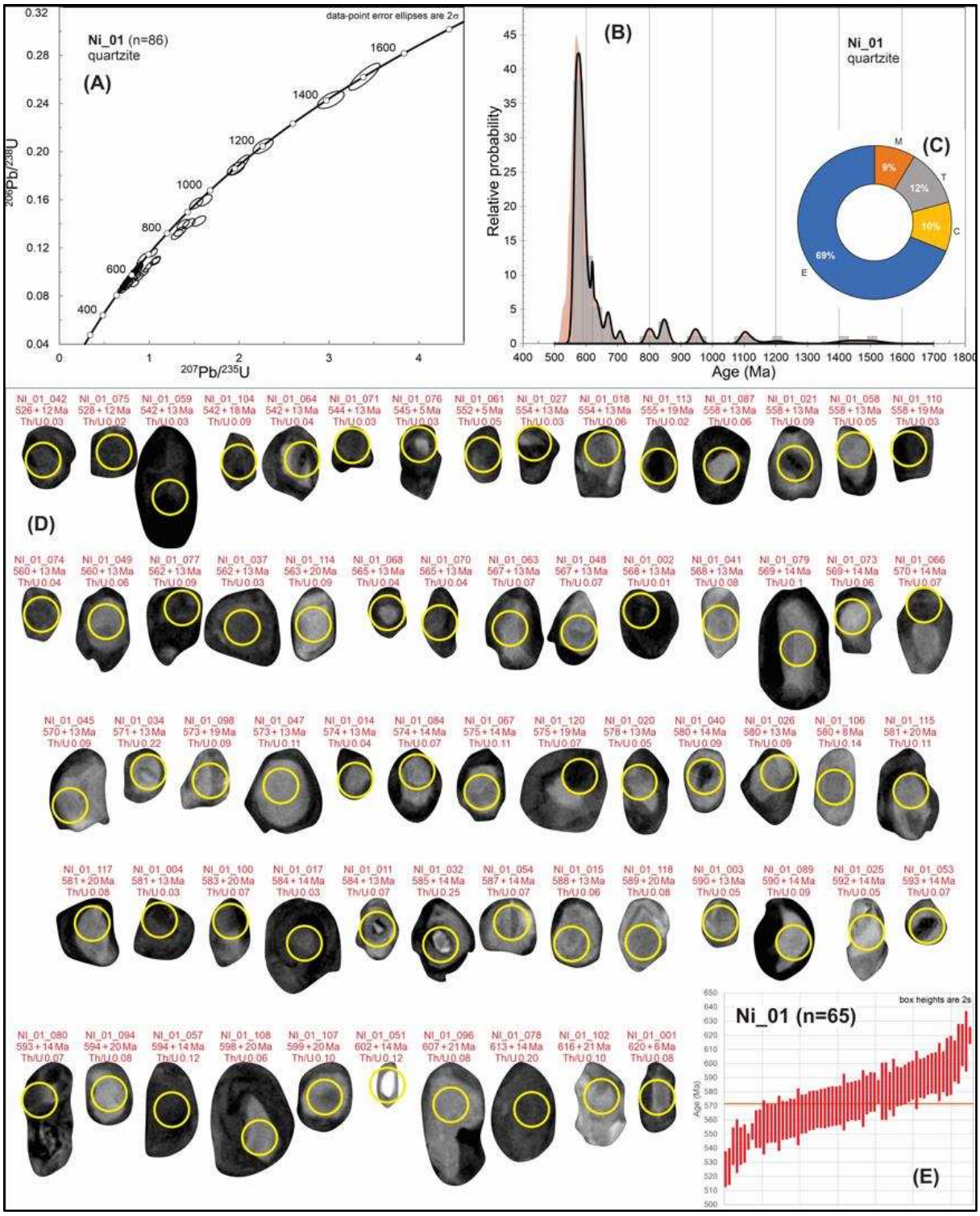

Figure 9 - Sample Ni_01 (quartzite). (A) Concordia diagram. (B) Relative age probability/histogram where shaded red area reflects the histogram for all data, while the full black line together with the grey columns represents solely zircons interpreted as detrital (refer to discussion topic 5.1). (C) Sector diagram with detrital zircon distribution (M=Mesoproterozoic; T=Tonian; C=Cryogenian; E=Ediacaran). (D) Selected

cathodoluminescence images of zircon grains between 490 and 625 Ma (yellow circles mark analysed spots for U-Pb). (E) Age distribution in error bars graph. Colour reflects morphological interpretation: black/grey=detrital and red=metamorphic.

4.4 - Lu-Hf geochronology:

LA-ICP-MS Lu-Hf analyses have been conducted on cordierite-sillimanite-garnet-biotite gneiss (CC_5A) and fine-grained biotite gneiss (CC_3B) samples from Morro Cara de Cão.

This study shows good distribution of $^{176}Hf/^{177}Hf$ within similar age ranges (Fig. 10b).

Both samples yield a highly homogeneous population that falls mainly below the depleted mantle model line (Fig. 10a)

The Neoproterozoic εHf values for the detrital zircons range from +5 to -18, which is consistent with a source from an ancient magmatic arc. In the Ediacaran period, the population varies between -6 and -17; in the Cryogenian it ranges from +6 to -29, and in the Tonian from +2 to -17. Between 1000-600 Ma, there appears to be a trend towards increasingly crustal signature. The εHf values of zircons from the Mesoproterozoic and Paleoproterozoic cluster around either close to -15 or near 0, with one exception showing an εHf of +9.

Through Lu-Hf isotopes, it was possible to confirm the detrital nature for the zircon population from 623-609 Ma (note the vertical distribution for this age range in Fig. 10b).

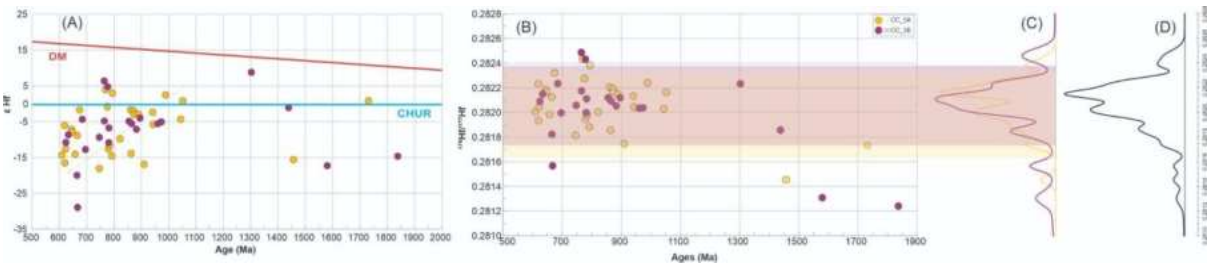

Figure 10 - (A) εHf versus individual ages (Ma) for samples CC_5A and CC_3B. Note down-left trend for Neoproterozoic data. Blue = CHUR (Chondritic Uniform Reservoir); red = DM (Depleted mantle). (B)$^{176}Hf/^{177}Hf$ ratio versus individual ages (Ma); (C, D) Probability density plots histograms for the distribution of $^{176}Hf/^{177}Hf$ for samples CC_5A and CC_3B (C) and for the studied basin (both samples combined) (D).

5 – Discussion

5.1 - Detrital and metamorphic ages on high-T terranes

The metamorphic peak of the Oriental Terrane is at least 850°C (Kühn *et al.*, 2004), several degrees above the closure temperature of zircon for U-Pb system (Zheng *et al.*, 2005). Therefore, in order to perform source analysis for detrital zircons from the paragneisses, we need to go deeply into the discussion about the origin of the crystals. It is critical to understand the detrital-metamorphic limit in high-T terranes. Our data shows that this is not a simple

formula. Although these paragneisses are intruded by magmatic units younger than 570 Ma, we found zircons of magmatic internal morphology (oscillatory growth) younger than this age. From field geology, we conclude that it is impossible to have detrital ages younger than 570 Ma. In this study, the internal structures of the zircon in cathodoluminescence images did not provide good evidence for distinguishing between detrital and metamorphic ages (Fig. 7d; Fig. 8d; Fig. 9d). The data suggest an apparent alternation between detrital and metamorphic crystals, which is not geologically plausible. In addition, Th/U ratios are also not useful. The zircon crystals that are metamorphic, younger than 570 Ma, in the paragneisses show Th/U above 0.1, implying that the composition of the rock is controlling this ratio. This evidence goes against the literature that adds that the metamorphic zircons should have Th/U ratios below 0.1. On the other hand, in the quartzite sample all metamorphic zircons (younger than 570 Ma) have Th/U ratios below 0.1. This confirms that the bulk composition of the rocks controls this ratio. To complete this, the presumed detrital zircons from the quartzite (above 570 Ma old) also present low Th/U ratios, equivalent to metamorphic origin, but some show oscillatory zoning.

Several authors point out that the Pb-loss process can be a reason for the disturbances on the zircon crystals. There are different possible causes for Pb-diffusion in crystalline zircon: thermal diffusion of Pb (Mezger e Krogstad, 1997; Cherniak e Watson, 2001), radiation damage annealing (Nasdala *et al.*, 2001; Geisler *et al.*, 2007), hydrothermal fluids (Hoskin e Black, 2000; Rubatto, 2002), zircon recrystallization (Geisler, 2002; Flowers *et al.*, 2006) and metamictization (Murakami *et al.*, 1991; Pidgeon, 1992). Our Cambrian-Ediacaran crystals show evidence for potential Pb-loss. The apparent intercalation between zircons with detrital and metamorphic morphologies, as well as an inconclusive Th/U distribution corroborate for this interpretation. The presence of garnet in Rio de Janeiro's paragneisses and quartzite is a possible contributor to Pb-diffusion process once the expulsion of zircon elements can happen during garnet growth (Rubatto, 2002; Kelly e Harley, 2005; Rubatto *et al.*, 2013; O'Brien e Miller, 2014).

Considering that the usual criteria to distinguish detrital and metamorphic zircons are not effective in the area, we could only use the field geology to identify the minimum age of sedimentation for the paragneisses protoliths. São Fidélis basin is intruded by Cambrian-Ediacaran magmatic intrusions, representing around 150 myr of arcs, syn- and post- orogenic activity (Valeriano *et al.,* 2011; Martins *et al.*, 2022; Vieira *et al.*, 2022). There are geological constraints in the area that we can start using (Fig. 2). Facoidal orthogneiss intrudes São Fidélis

meta-sediments and was submitted to the same metamorphic episode. Therefore, its crystallisation age can be no older than the youngest detrital zircon from the basin.

We imply that this is a case of lead loss associated with continuous very slow cooling (Ashwal *et al.*, 1999). Pb-loss and long-lived magmatic domains in time proximity to metamorphism (Brasiliano metamorphic event) required us to find alternatives on how to get the minimum age of sedimentation.

5.2 - Provenance analysis of the São Fidélis Basin

Considering the above, separating detrital populations from the three studied samples we pursued the potential source areas, in order to comprehend the tectonic environment of the original basin in which these sediments were deposited.

The pre-Neoproterozoic detrital populations are rare, with one minor peak at 2.0-1.9 Ga and another at 1.45 Ga (Fig. 11a). These Paleoproterozoic sources are widespread in the Angola Craton and the Cabo Frio Tectonic Domain (Fig. 1). The Mesoproterozoic sources are also abundant at the Angola Craton, part of the anorogenic magmatism within the Kunene Complex (Milani *et al.*, 2022; McCourt *et al.*, 2013), one example is the Red Granite suite (1442-1370 Ma). On the Brazilian side, Mesoproterozoic sources are not common, but the Apiaí Terrane, in the southern Ribeira belt, is one strong candidate (Cabrita *et al.*, 2023; Basei *et al.*, 2003; Hartmann *et al.*, 2000). In the end of the Mesoproterozoic, after 1.25 Ga, the frequency of minor populations grew (Fig. 11a). These ages of 1.0-1.2 Ga can be partially attributed to a source in the Kunene Igneous Complex in the Angola shield (1400-1100 Ma - Fig. 1a).

The significant age peaks of detrital zircons occur in the Neoproterozoic (Fig. 11a): 980-930 Ma, 856-838 Ma, 800-740 Ma and 690-580 Ma, the latter is the most abundant population. These detrital populations tend to coincide with the age of the magmatic events within the Oriental Terrane (Fig. 1b).Therefore, we interpret the magmatic arcs Serra da Bolívia, Rio Negro and Serra da Prata as possible sources (Peixoto *et al.*, 2017; Tupinambá *et al.*, 2012; Heilbron e Machado, 2003). The Tonian age peak (856-838 Ma) is coeval with the Serra da Prata Arc. The Rio Negro Arc age range (630-595 Ma) and the Serra da Bolívia Arc (595-570 Ma) are both entirely consistent with one of the main peaks, indicating a high probability that they were important source rocks. The age peak of 800-740 Ma is coeval with the Tonian orogenesis of the Embu Terrane, 850-760 Ma, in southern Ribeira Orogen (Campanha *et al.*, 2023). The oldest Neoproterozoic detrital age peak, of 980-930 Ma, could

be correlated with 1000-910 Ma bimodal magmatism at the West Congo Belt (Tack *et al.*, 2001).

The Lu-Hf data from the Neoproterozoic detrital zircons corroborate with the hypothesis that these major sources could be magmatic arcs, because of the wide variations on the εHf values. The detrital zircons that are possible derived from the Rio Negro and Serra da Bolivia magmatic arcs show εHf varying from -2 to -17 (Fig. 10a). For the detrital zircons coeval with the activity of the Serra da Prata arc, we have only one εHf analysis of -2. The age peak equivalent with the Tonian orogenesis from the Embu Terrane, 800-740 Ma, presents εHf values varying from -18 to +6. Within this interval, positive values are observed in the 794-764 Ma zircons, suggesting a contribution from an oceanic source. This reinforces that the source had both juvenile and crustal signatures, therefore could be a magmatic arc. The detrital zircons from the age interval 980-930 Ma have εHf varying from -6 to -2.

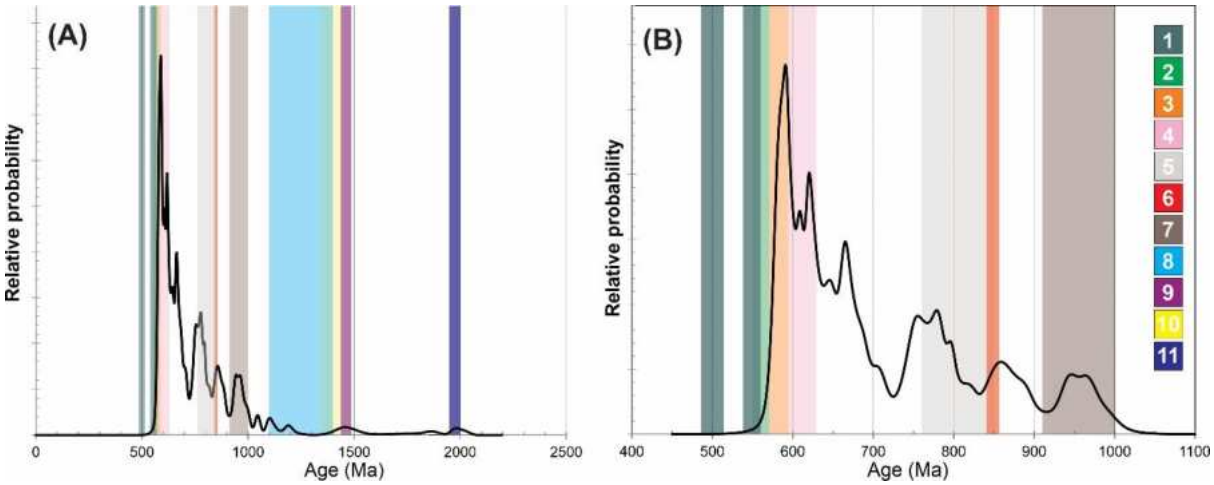

Figure 11 - Histograms for U-Pb ages from all (A) and only Neoproterozoic (B) studied samples. Coloured zones represent different geological event crystallisation ages: 1) Late- to post-orogenic magmatism (570-540 Ma and 510-480 Ma) (Martins et al., 2022). 2) Facoidal Orthogneiss (570-560 Ma) (Martins et al., 2021). 3) Serra da Bolívia Arc (595-570 Ma) (Peixoto et al., 2017). 4) Rio Negro Arc (630-595 Ma) (Heilbron et al., 2020; Heilbron and Machado, 2003; Tupinambá et al., 2012). 5) Embu Terrane (850-760 Ma) (Campanha et al., 2023) 6) Serra da Prata Arc (856-838 Ma) (Peixoto et al., 2017). 7) Early Neoproterozoic magmatism at the West Congo Belt (1000-910 Ma) (Tack et al., 2001). 8) Kunene Igneous Complex (1400-1100 Ma) (Becker et al., 2006; Carvalho et al., 2000; Kröner et al., 2004; Pereira et al., 2011; Seth et al., 2003). 9) Apiaí Terrane (1484-1434 Ma) (Basei et al., 2003; Cabrita et al., 2023; Hartmann et al., 2000). 10) Red Granite suite (1442-1370 Ma) (Milani et al., 2022; McCourt et al., 2013). 11) Cabo Frio Tectonic Domain and Angola Craton (2100-1700 Ma) (Schmitt et al., 2004, 2016; Ferreira et al., 2024; Kröner et al., 2010).

5.3 - Tectonic implications:

The U-Pb and combined Lu-Hf data here presented from the para-derived high-grade rocks of Rio de Janeiro city provide insights on the paleogeographic context of the Oriental Terrane, further clarifying its relationship with nearby crustal blocks and their influence on

regional tectonic evolution. These paragneisses are part of the São Fidélis Group, a large geological unit that comprises most of this terrane (Fig. 01). We compared the detrital spectra of our samples with the other U-Pb data from the São Fidélis Group (Fig. 12a). Our data presents all sources previously registered for São Fidélis Group (Fernandes *et al.*, 2015, Lobato *et al.*, 2015, Peixoto *et al.*, 2022), with the exception of the Neoarchean detrital peak. On the other hand, our detrital zircon data, register a new peak of 1.5-1.2 Ga. In addition, the detrital zircons here analysed are also more abundant than the previous analyses in the age intervals of 800-760 and 880-820 Ma.

We also compared our data with the other Neoproterozoic basins, preserved in the neighbouring Cabo Frio Tectonic Domains (Fig. 1): the Palmital (Fernandes *et al.*, 2015) and the Búzios (De Freitas *et al.*, 2024, Fernandes *et al.*, 2015) basins (Fig. 12a). It is noteworthy that our data do not have the Neoarchean peak, and that it shows more abundance of registered Mesoproterozoic ages between 1.6-1.2 Ga.

Lu-Hf data also allows a comparison with the existing information on São Fidélis (Fernandes *et al.*, 2015), Palmital (Fernandes *et al.*, 2015) and Búzios (De Freitas *et al.*, 2024, Fernandes *et al.*, 2015) basins. Our data is coherent with the distribution previously observed for São Fidélis basin, presenting most εHf values of 0 to -20 with exceptions above the CHUR line (Fig. 12b). Data from the Palmital basin plots similarly. However, εHf data from the Búzios basin show a more juvenile Neoproterozoic signature, mostly positive. Supported by U-Pb and Lu-Hf on detrital zircons, we conclude that the São Fidélis basin and the Palmital basin are probably the same, whereas the Búzios basin is separate and different.

The studied basin registered a very small period of time -even possibly overlapped- between the youngest detrital zircon deposited and the beginning of metamorphic zircon growth. When analysing the difference between crystallisation and depositional zircon ages we can interpret aspects of the basin tectonics. All three samples plot within the collisional to the convergent margin basin criteria (Cawood *et al.*, 2012) (Fig. 13) and previous data on São Fidélis basin plot closely to convergent margin (Capistrano *et al.*, 2017). In this situation of syn-sedimentary magmatism, where the main source area is contained in the same terrane as the basin (Oriental Terrane), the most probable interpretation would be a forearc or a back-arc basin environment.

Furthermore, metamorphic conditions calculated for these paragneisses are of high-temperature (Kuhn *et al.*, 2004). In average conditions on the lithosphere with geothermal gradient ~50ºC/km (Kolawole and Evenick, 2023), it would require the rock to go to great depth in a short amount of time. Consequently, the way for our sedimentary basin to be able to

reach high temperatures in such a short time would be in a high thermal flux terrane, where isothermals are shallower (Fossen *et al.*, 2017, Thompson, 1984). In a hot-orogen, the basin would need to subsidise significantly less to reach metamorphic conditions (Bento dos Santos *et al.*, 2015). Hot-orogen conditions associated with magmatic arcs influence are also supported by the εHf distribution from juvenile to crustal observed in this work. Therefore, suggesting it is the case of a sin-orogenic basin.

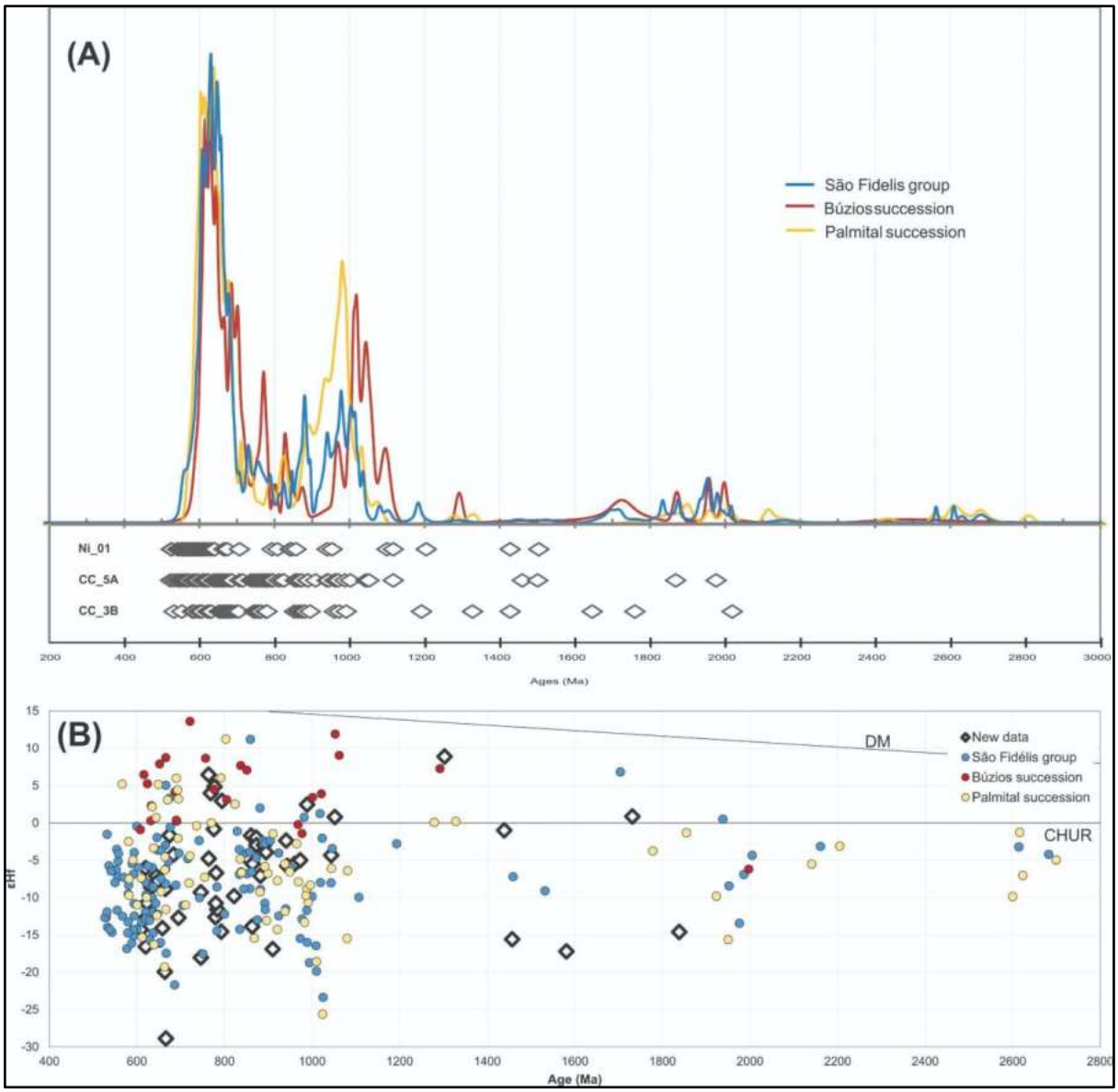

Figure 12 - (A) Relative density plot for São Fidélis group, Búzios succession and Palmital group compiled from Fernandes et al. (2015); Lobato et al. (2015); De Araujo Peixoto et al. (2022); and Freitas et al. (2024). Zircon age plot (grey rhombus) distribution for samples in this work. (B) εHf x Age (Ma) plot for new data from this study and for São Fidélis group, Búzios succession and Palmital group compiled from Fernandes et al. (2015) and de Freitas et al. (2024).

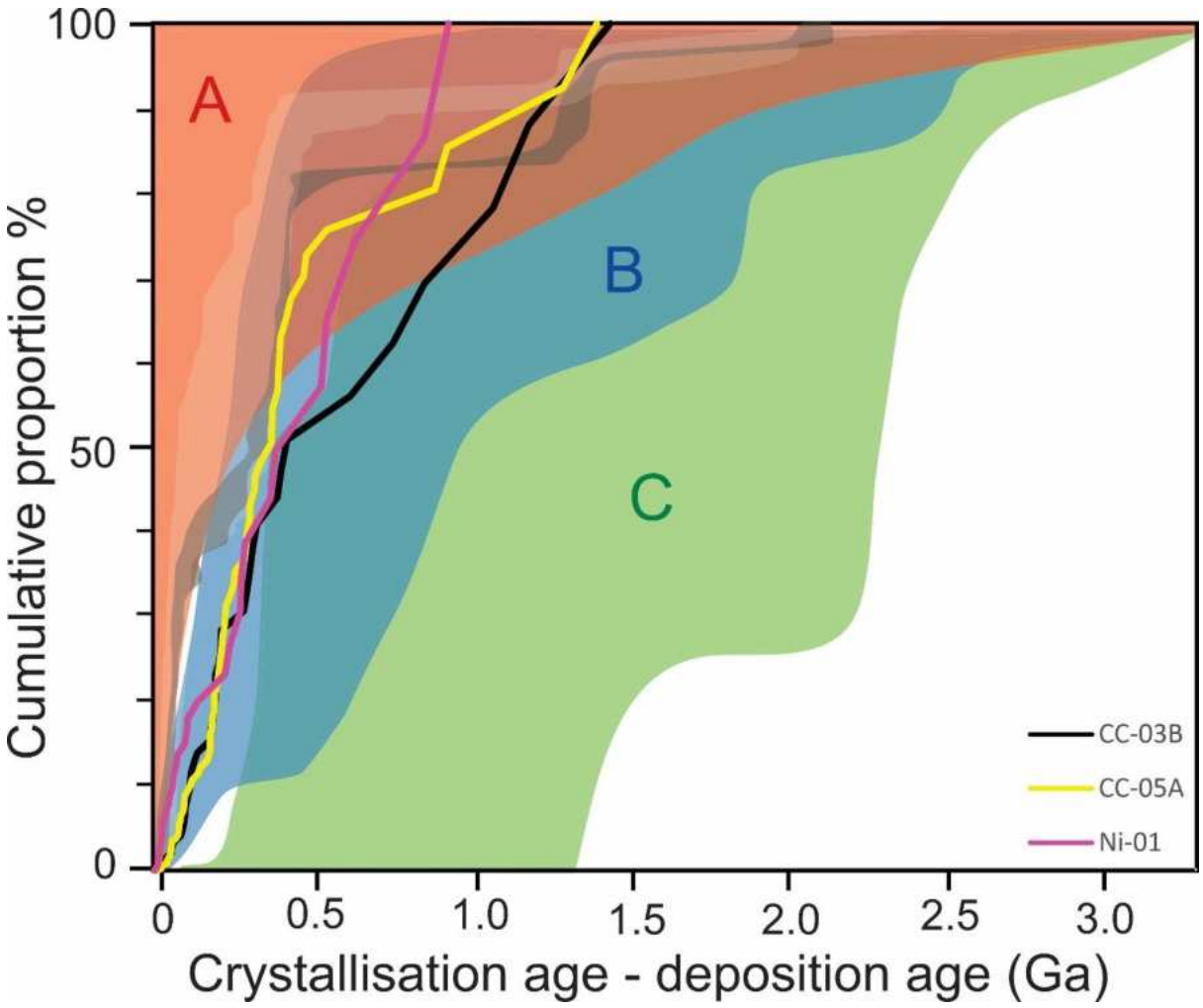

Figure 13 - Diagram of ages of detrital zircons X sedimentation age of the basin (570 Ma) of samples in this study. Convergent (A: red field), collisional (B: blue field) and extensional basins (C: green field) (Cawood et al., 2012). Dark grey shaded area represents previous data for São Fidélis group and white shaded are represents previous data for Palmital succession (Capistrano et al., 2017).

6. Conclusions:

Based on the data and discussions presented in this study, utilizing U-Pb and Lu-Hf methodologies alongside petrology, fieldwork, and a comprehensive literature review, several key points can be highlighted as conclusions:

(1) The studied basin formed in a convergent margin setting, characterized as a hot-orogen. We suggest that this basin is either a retro-arc or fore-arc basin.

(2) The hot-orogen nature of the basin led to slow cooling, which is interpreted as the main cause of Pb loss in the zircons. This process may have affected the U-Pb analysis results, as indicated by inconclusive morphological patterns, abnormal Th/U distribution (relative to the typical metamorphic limit of 0.1), and presence of garnet in the mineral assemblage, partially supporting this interpretation.

(3) The late Ediacaran zircons in the samples are of both metamorphic and detrital origin, reflecting the age and composition of the source rock. The youngest detrital grain cannot be younger than 570 Ma, based on its field relationship with the intrusive plutonic facoidal orthogneiss, which crystallized at this age.

(4) The main detrital populations align with the ages of magmatic events from the Oriental Terrane, in which the São Fidélis Group is also included. The age peaks of 856–838 Ma, 800–740 Ma, and 690–580 Ma were correlated, respestively, with the age domains of the Serra da Prata Arc, the Embu Terrane, and the Rio Negro Arc along with the Serra da Bolívia Arc. Minor peaks were observed at 2.0–1.9 Ga and 1.45 Ga. An age range not previously recorded for these rocks in the literature was identified between 1.5–1.2 Ga.
(5) The εHf data vary from juvenile to crustal signatures for the Neoproterozoic, consistent with the interpretation of a magmatic arc source.
(6) The São Fidélis and Palmital basins exhibit strong similarities in detrital zircon U-Pb and Lu-Hf values, suggesting that they may have been part of the same basin.

Acknowledgements

We thank the financial support of Petrobras/CENPES in cooperation with the Federal University of Rio de Janeiro (UFRJ). This paper is a contribution to the project "Geodinâmica da litosfera continental do Gondwana SW - o embasamento do sistema de riftes do Atlântico Sul" (COPPETEC IGEO 22661). We also thank FAPERJ for the financial support on "Apoio as Instituições de Pesquisa Sediadas no RJ" (E-26/010.101120/2018).

V. CONCLUSÃO

Com base nos dados e discussões apresentados neste trabalho, utilizando metodologia U-Pb e Lu-Hf juntamente com petrologia, trabalho de campo e estudo bibliográfico, é possível destacar alguns pontos como conclusão:

(1) A bacia estudada se formou em um contexto de margem convergente, caracterizando-se como um orógeno quente. Sugerimos que essa bacia seja de retroarco ou antearco.

(2) A natureza de orógeno quente da bacia leva a um resfriamento lento, interpretado como a principal causa da perda de Pb em zircão. Esse processo pode ter interferido nos resultados das análises U-Pb, evidenciado por padrões morfológicos inconclusivos, distribuição anormal de Th/U (em relação ao limite metamórfico típico de 0,1), e pela presença de granada na assembleia mineralógica, suportando parcialmente essa interpretação.

(3) Os grão de zircão do final do Ediacarano presentes nas amostras são tanto de origem metamórfica quanto detrítica, refletindo a idade e composição da rocha-fonte. O grão detrítico mais jovem não pode ser mais recente que 570 Ma, em função de sua relação de campo com o ortognaisse facoidal plutônico intrusivo, cuja cristalização ocorreu nessa idade.

(4) As principais populações detríticas coincidem com as idades dos eventos magmáticos do Terreno Oriental, no qual o Grupo São Fidélis também está inserido. Os picos de idade de 856-838 Ma, 800-740 Ma e 690-580 Ma foram correlacionados, respectivamente, com os domínios de idade do Arco Serra da Prata, do Terreno Embu e do Arco Rio Negro juntamente com o Arco Serra da Bolívia. Picos menos expressivos foram observados em 2,0-1,9 Ga e 1,45 Ga. Um intervalo de idade não registrado anteriormente para essas rochas na bibliografia foi identificado em 1,5-1,2 Ga.

(5) Os dados de εHf variam de assinaturas juvenis a crustais para o Neoproterozoico, o que é coerente com a interpretação de uma fonte de arco magmático.

(6) As bacias de São Fidélis e Palmital mostram grande semelhança nos valores U-Pb e Lu-Hf de zircão detrítico, o que sugere que ambas podem ter sido parte da mesma bacia.

REFERÊNCIAS BIBLIOGRÁFICAS

ANDERSEN, T. "Detrital zircons as tracers of sedimentary provenance: limiting conditions from statistics and numerical simulation", **Chemical Geology**, v. 216, n. 3–4, p. 249–270, mar. 2005. DOI: 10.1016/j.chemgeo.2004.11.013.

ANDERSEN, T., ANDERSSON, U. B., GRAHAM, S., *et al.* "Granitic magmatism by melting of juvenile continental crust: new constraints on the source of Palaeoproterozoic granitoids in Fennoscandia from Hf isotopes in zircon", **Journal of the Geological Society**, v. 166, n. 2, p. 233–247, mar. 2009. DOI: 10.1144/0016-76492007-166.

BARHAM, M., KIRKLAND, C. L., HANDOKO, A. D. "Understanding ancient tectonic settings through detrital zircon analysis", **Earth and Planetary Science Letters**, v. 583, p. 117425, 1 abr. 2022. DOI: 10.1016/j.epsl.2022.117425.

BASEI, M. A. S., SIGA JR., O., KAULFUSS, G. A., *et al.* "Geochronology and isotope geochemistry of Votuverava and Perau Mesoproterozoic basins, southern Ribeira Belt, Brazil", **Geochronology and isotope geochemistry of Votuverava and Perau Mesoproterozoic basins, southern Ribeira Belt, Brazil**, 2003.

BECKER, T., SCHREIBER, U., KAMPUNZU, A. B., *et al.* "Mesoproterozoic rocks of Namibia and their plate tectonic setting", **Journal of African Earth Sciences**, v. 46, n. 1–2, p. 112–140, set. 2006. DOI: 10.1016/j.jafrearsci.2006.01.015.

BENTO DOS SANTOS, T. M., TASSINARI, C. C. G., FONSECA, P. E. "Diachronic collision, slab break-off and long-term high thermal flux in the Brasiliano–Pan-African orogeny: Implications for the geodynamic evolution of the Mantiqueira Province", **Precambrian Research**, v. 260, p. 1–22, maio 2015. DOI: 10.1016/j.precamres.2014.12.018.

BOUVIER, A., VERVOORT, J. D., PATCHETT, P. J. "The Lu–Hf and Sm–Nd isotopic composition of CHUR: Constraints from unequilibrated chondrites and implications for the bulk composition of terrestrial planets", **Earth and Planetary Science Letters**, v. 273, n. 1, p. 48–57, 30 ago. 2008. DOI: 10.1016/j.epsl.2008.06.010.

CABRITA, D. I. G., FALEIROS, F. M., CAMPANHA, G. A. C., *et al.* "Meso- to Neoproterozoic terrane accretion: Insights from juvenile mafic magmatism from the Votuverava Group and Embu Complex, southern Ribeira Belt, Brazil", **Precambrian Research**, v. 386, p. 106970, mar. 2023. DOI: 10.1016/j.precamres.2023.106970.

CAMPANHA, G. A. C., FALEIROS, F. M., CABRITA, D. I. G., *et al.* "The southern Ribeira Belt in Western Gondwana: a record of a long-lived continental margin and terrane collage", **Journal of South American Earth Sciences**, v. 127, p. 104404, 1 jul. 2023. DOI: 10.1016/j.jsames.2023.104404.

CAPISTRANO, G. G., SCHMITT, R. S., MEDEIROS, S. R., *et al.* "Evidence of a Neoproterozoic active continental margin - Geochemistry and isotope geology of high-grade paragneiss from the Ribeira Orogen, SE Brazil", **Journal of South American Earth Sciences**, v. 77, p. 170–184, ago. 2017. DOI: 10.1016/j.jsames.2017.05.006.

CARVALHO, H., TASSINARI, C., ALVES, P. H., *et al.* "Geochronological review of the Precambrian in western Angola: links with Brazil", **Journal of African Earth Sciences**, v. 31,

n. 2, p. 383–402, ago. 2000. DOI: 10.1016/S0899-5362(00)00095-6.

CAWOOD, P. A., HAWKESWORTH, C. J., DHUIME, B. "Detrital zircon record and tectonic setting", **Geology**, v. 40, n. 10, p. 875–878, out. 2012. DOI: 10.1130/G32945.1.

CONDIE, K. C., ARNDT, N., DAVAILLE, A., *et al.* "Zircon age peaks: Production or preservation of continental crust?", **Geosphere**, v. 13, n. 2, p. 227–234, 1 abr. 2017. DOI: 10.1130/GES01361.1.

CORFU, F., HANCHAR, J. M., HOSKIN, P. W. O., *et al.* "Atlas of Zircon Textures", **Reviews in Mineralogy and Geochemistry**, v. 53, n. 1, p. 469–500, 2 jan. 2003. DOI: 10.2113/0530469.

DE FREITAS, N. C., HEILBRON, M., ALMEIDA, J., *et al.* "New U-Pb and Hf data of the contact region between the Oriental and Cabo Frio terranes, Central Ribeira Belt, Brazil: Implications for the closure of the Ediacaran-Cambrian oceanic space", **Precambrian Research**, v. 401, p. 107272, 1 fev. 2024. DOI: 10.1016/j.precamres.2023.107272.

FERNANDES, G. L. D. F., SCHMITT, R. D. S., BONGIOLO, E. M., *et al.* "Unraveling the tectonic evolution of a Neoproterozoic–Cambrian active margin in the Ribeira Orogen (Se Brazil): U–Pb and Lu–Hf provenance data", **Precambrian Research**, v. 266, p. 337–360, set. 2015. DOI: 10.1016/j.precamres.2015.05.017.

FERREIRA, E., LEHMANN, J., FELICIANO RODRIGUES, J., *et al.* "Zircon U-Pb and Lu-Hf isotopes reveal the crustal evolution of the SW Angolan Shield (Congo Craton)", **Gondwana Research**, v. 131, p. 317–342, jul. 2024. DOI: 10.1016/j.gr.2024.03.010.

FOSSEN, H., CAVALCANTE, G. C., DE ALMEIDA, R. P. "Hot Versus Cold Orogenic Behavior: Comparing the Araçuaí-West Congo and the Caledonian Orogens", **Tectonics**, v. 36, n. 10, p. 2159–2178, out. 2017. DOI: 10.1002/2017TC004743.

GEHRELS, G. "Detrital Zircon U-Pb Geochronology Applied to Tectonics", **Annual Review of Earth and Planetary Sciences**, v. 42, n. Volume 42, 2014, p. 127–149, 30 maio 2014. DOI: 10.1146/annurev-earth-050212-124012.

GEHRELS, G., "Detrital Zircon U-Pb Geochronology: Current Methods and New Opportunities". **Tectonics of Sedimentary Basins**, [S.l.], John Wiley & Sons, Ltd, 2011. p. 45–62. DOI: 10.1002/9781444347166.ch2. Disponível em: https://onlinelibrary.wiley.com/doi/abs/10.1002/9781444347166.ch2. Acesso em: 26 set. 2024.

GERALDES, M. C. *et al.* "U-Pb and Lu-Hf calibration of the new LA-ICP-MS multilab at Rio de Janeiro state university.", **The 9th International Conference on the Analysis of Geological and Environmenta l Materials.**, n. Leoben-Austria, 2015.

GRIFFIN, W. L., PEARSON, N. J., BELOUSOVA, E., *et al.* "The Hf isotope composition of cratonic mantle: LAM-MC-ICPMS analysis of zircon megacrysts in kimberlites", **Geochimica et Cosmochimica Acta**, v. 64, n. 1, p. 133–147, 1 jan. 2000. DOI: 10.1016/S0016-7037(99)00343-9.

HACKSPACHER, P. C., FETTER, A. H., EBERT, H. D., *et al.* "Magmatismo há ca. 660 - 640 Ma no Domínio Socorro: registros de convergência pré-colisional na aglutinação do Gondwana

Ocidental", **Geologia USP. Série Científica**, v. 3, n. 1, p. 85–96, 1 ago. 2003. DOI: 10.5327/S1519-874X2003000100007.

HARLEY, S. L., KELLY, N. M., MÖLLER, A. "Zircon Behaviour and the Thermal Histories of Mountain Chains", **Elements**, v. 3, n. 1, p. 25–30, 1 fev. 2007. DOI: 10.2113/gselements.3.1.25.

HARTMANN, L. A., SANTOS, J. O. S., MCNAUGHTON, N. J., *et al.* "Ion microprobe (SHRIMP) dates complex granulite from Santa Catarina, southern Brazil", **Anais da Academia Brasileira de Ciências**, v. 72, n. 4, p. 559–572, dez. 2000. DOI: 10.1590/S0001-37652000000400007.

HEILBRON, M., MACHADO, N. "Timing of terrane accretion in the Neoproterozoic–Eopaleozoic Ribeira orogen (se Brazil)", **Precambrian Research**, v. 125, n. 1, p. 87–112, 15 jul. 2003. DOI: 10.1016/S0301-9268(03)00082-2.

HEILBRON, M., SILVA, L. G. D. E., ALMEIDA, J. C. H. D., *et al.* "Proterozoic to Ordovician geology and tectonic evolution of Rio de Janeiro State, SE-Brazil: insights on the central Ribeira Orogen from the new 1:400,000 scale geologic map", **Brazilian Journal of Geology**, v. 50, n. 2, p. e20190099, 2020. DOI: 10.1590/2317-4889202020190099.

HEILBRON, M., TUPINAMBÁ, M., VALERIANO, C. de M., *et al.* "The Serra da Bolívia complex: The record of a new Neoproterozoic arc-related unit at Ribeira belt", **Precambrian Research**, v. 238, p. 158–175, 1 nov. 2013. DOI: 10.1016/j.precamres.2013.09.014.

HEILBRON, M., VALERIANO, C., PEIXOTO, C., *et al.* "Neoproterozoic magmatic arc systems of the central Ribeira belt, SE-Brazil, in the context of the West-Gondwana pre-collisional history: A review", **Journal of South American Earth Sciences**, v. 103, p. 102710, 1 nov. 2020. DOI: 10.1016/j.jsames.2020.102710.

HOSKIN, P. W. O., SCHALTEGGER, U. "The Composition of Zircon and Igneous and Metamorphic Petrogenesis", **Reviews in Mineralogy and Geochemistry**, v. 53, n. 1, p. 27–62, 2 jan. 2003. DOI: 10.2113/0530027.

JIAN, D., WILLIAMS, S. E., YU, S., *et al.* "Quantifying the Link Between the Detrital Zircon Record and Tectonic Settings", **Journal of Geophysical Research: Solid Earth**, v. 127, n. 9, p. e2022JB024606, 2022. DOI: 10.1029/2022JB024606.

KELLY, N. M., HARLEY, S. L. "An integrated microtextural and chemical approach to zircon geochronology: refining the Archaean history of the Napier Complex, east Antarctica", **Contributions to Mineralogy and Petrology**, v. 149, n. 1, p. 57–84, mar. 2005. DOI: 10.1007/s00410-004-0635-6.

KOLAWOLE, F., EVENICK, J. C. "Global distribution of geothermal gradients in sedimentary basins", **Geoscience Frontiers**, v. 14, n. 6, p. 101685, nov. 2023. DOI: 10.1016/j.gsf.2023.101685.

KRÖNER, A., ROJAS-AGRAMONTE, Y., HEGNER, E., *et al.* "SHRIMP zircon dating and Nd isotopic systematics of Palaeoproterozoic migmatitic orthogneisses in the Epupa Metamorphic Complex of northwestern Namibia", **Precambrian Research**, v. 183, n. 1, p. 50–69, nov. 2010. DOI: 10.1016/j.precamres.2010.06.018.

KRÖNER, S., KONOPÁSEK, J., KRÖNER, A., *et al.* "U-Pb and Pb-Pb zircon ages for metamorphic rocks in the Kaoko Belt of Northwestern Namibia: A Palaeo- to Mesoproterozoic basement reworked during the Pan-African orogeny", **South African Journal of Geology**, v. 107, n. 3, p. 455–476, 1 set. 2004. DOI: 10.2113/107.3.455.

KÜHN, A., STÜWE, K., TROUW, R. A. J. "Metamorphic Evolution of the Ribeira Belt: Evidence from Outcrops in the Rio de Janeiro Area, Brazil", **Journal of Petrology**, v. 45, n. 11, p. 2303–2323, 12 ago. 2004. DOI: 10.1093/petrology/egh058.

LOBATO, M., HEILBRON, M., TORÓS, B., *et al.* "Provenance of the Neoproterozoic high-grade metasedimentary rocks of the arc-related Oriental Terrane of the Ribeira belt: Implications for Gondwana amalgamation", **Journal of South American Earth Sciences**, v. 63, p. 260–278, nov. 2015. DOI: 10.1016/j.jsames.2015.07.019.

LUDWIG, K. "Isoplot 3.0", **Special Publication**, 1 jan. 2003.

MARTINS, G. G., MENDES, J. C., SCHMITT, R. D. S., *et al.* "Long-term magmatism in the Ribeira Orogen, Western Gondwana: SHRIMP U-Pb and O isotope data for two Ediacaran-Cambrian magmatic events in the Rio de Janeiro area", **Precambrian Research**, v. 383, p. 106908, dez. 2022. DOI: 10.1016/j.precamres.2022.106908.

MARTINS, G., MENDES, J. C., SCHMITT, R. D. S., *et al.* "Unravelling source and tectonic environment of an Ediacaran magmatic province from southeast Brazil: Insights from geochemistry and isotopic investigation", **Lithos**, v. 404–405, p. 106428, dez. 2021. DOI: 10.1016/j.lithos.2021.106428.

MCCOURT, S., ARMSTRONG, R. A., JELSMA, H., *et al.* "New U–Pb SHRIMP ages from the Lubango region, SW Angola: insights into the Palaeoproterozoic evolution of the Angolan Shield, southern Congo Craton, Africa", **Journal of the Geological Society**, v. 170, n. 2, p. 353–363, mar. 2013. DOI: 10.1144/jgs2012-059.

MCLAREN, A. C., GERALD, J. D. F., WILLIAMS, I. S. "The microstructure of zircon and its influence on the age determination from Pb/U isotopic ratios measured by ion microprobe", **Geochimica et Cosmochimica Acta**, v. 58, n. 2, p. 993–1005, jan. 1994. DOI: 10.1016/0016-7037(94)90521-5.

MILANI, L., LEHMANN, J., BYBEE, G. M., *et al.* "Geochemical and geochronological constraints on the Mesoproterozoic Red Granite Suite, Kunene AMCG Complex of Angola and Namibia", **Precambrian Research**, v. 379, p. 106821, 1 set. 2022. DOI: 10.1016/j.precamres.2022.106821.

MOECHER, D., SAMSON, S. "Differential zircon fertility of source terranes and natural bias in the detrital zircon record: Implications for sedimentary provenance analysis", **Earth and Planetary Science Letters**, v. 247, n. 3–4, p. 252–266, 30 jul. 2006. DOI: 10.1016/j.epsl.2006.04.035.

PEIXOTO, C. A., HEILBRON, M., RAGATKY, D., *et al.* "Tectonic evolution of the Juvenile Tonian Serra da Prata magmatic arc in the Ribeira belt, SE Brazil: Implications for early west Gondwana amalgamation", **Precambrian Research**, v. 302, p. 221–254, nov. 2017. DOI: 10.1016/j.precamres.2017.09.017.

PEIXOTO, C. A., LOBATO, M., DE FREITAS, N. C., *et al.* "Geochronological constraints of high-grade metasedimentary rocks of the Italva and Costeiro basins: Reconstructing the Outer Magmatic Arc System of the ribeira belt, SE Brazil", **Precambrian Research**, v. 382, p. 106879, nov. 2022. DOI: 10.1016/j.precamres.2022.106879.

PEREIRA, E., TASSINARI, C. C. G., RODRIGUES, J. F., *et al.* "New data on the deposition age of the volcano-sedimentary Chela Group and its Eburnean basement: implications to postEburnean crustal evolution of the SW of Angola", **Comunicações geológicas**, v. 98, p. 29–40, 2011.

PIDGEON, R. T. "Recrystallisation of oscillatory zoned zircon: some geochronological and petrological implications", **Contributions to Mineralogy and Petrology**, v. 110, n. 4, p. 463–472, 1 maio 1992. DOI: 10.1007/BF00344081.

RUBATTO, D. "Zircon: The Metamorphic Mineral", **Reviews in Mineralogy and Geochemistry**, v. 83, n. 1, p. 261–295, 1 ago. 2017. DOI: 10.2138/rmg.2017.83.9.

RUBATTO, D., WILLIAMS, I. S., BUICK, I. S. "Zircon and monazite response to prograde metamorphism in the Reynolds Range, central Australia", **Contributions to Mineralogy and Petrology**, v. 140, n. 4, p. 458–468, 1 jan. 2001. DOI: 10.1007/PL00007673.

SCHALTEGGER, U., FANNING, C. M., GÜNTHER, D., *et al.* "Growth, annealing and recrystallization of zircon and preservation of monazite in high-grade metamorphism: conventional and in-situ U-Pb isotope, cathodoluminescence and microchemical evidence", **Contributions to Mineralogy and Petrology**, v. 134, n. 2, p. 186–201, 1 fev. 1999. DOI: 10.1007/s004100050478.

SCHMITT, R. D. S., TROUW, R., VAN SCHMUS, W. R., *et al.* "The tectonic significance of the Cabo Frio Tectonic Domain in the SE Brazilian margin: a Paleoproterozoic through Cretaceous saga of a reworked continental margin", **Brazilian Journal of Geology**, v. 46, n. suppl 1, p. 37–66, jun. 2016. DOI: 10.1590/2317-4889201620150025.

SCHMITT, R. S., TROUW, R. A. J., VAN SCHMUS, W. R., *et al.* "Late amalgamation in the central part of West Gondwana: new geochronological data and the characterization of a Cambrian collisional orogeny in the Ribeira Belt (SE Brazil)", **Precambrian Research**, v. 133, n. 1–2, p. 29–61, ago. 2004. DOI: 10.1016/j.precamres.2004.03.010.

SETH, B., ARMSTRONG, R. A., BRANDT, S., *et al.* "Mesoproterozoic U–Pb and Pb–Pb ages of granulites in NW Namibia: reconstructing a complete orogenic cycle", **Precambrian Research**, v. 126, n. 1–2, p. 147–168, set. 2003. DOI: 10.1016/S0301-9268(03)00193-1.

SILVA, L. C. D., MCNAUGHTON, N. J., HARTMANN, L. A., *et al.* "Zircon U-Pb shrimp dating of the Serra dos Órgãos and Rio de Janeiro gneissic granitic suites: implications for the (560 Ma) Brasiliano/Pan-African collage", **Revista Brasileira de Geociências**, v. 33, n. 2, p. 237–244, 1 jun. 2003. DOI: 10.25249/0375-7536.2003332237244.

SÖDERLUND, U., PATCHETT, P. J., VERVOORT, J. D., *et al.* "The 176Lu decay constant determined by Lu–Hf and U–Pb isotope systematics of Precambrian mafic intrusions", **Earth and Planetary Science Letters**, v. 219, n. 3–4, p. 311–324, mar. 2004. DOI: 10.1016/S0012-821X(04)00012-3.

TACK, L. *et al.* Early Neoproterozoic magmatism (1000–910 Ma) of the Zadinian and Mayumbian Groups (Bas-Congo): onset of Rodinia rifting at the western edge of the Congo craton. **Precambrian research**, v. 110, n. 1-4, p. 277-306, 2001.

TEDESCHI, M., LEONARDO ROSSI VIEIRA, P., KUCHENBECKER, M., *et al.* "Unravelling the protracted U-Pb zircon geochronological record of high to ultrahigh temperature metamorphic rocks: Implications for provenance investigations", **Geoscience Frontiers**, v. 14, n. 2, p. 101515, mar. 2023. DOI: 10.1016/j.gsf.2022.101515.

THOMPSON, A. B., "Geothermal Gradients Through Time". In: HOLLAND, H. D., TRENDALL, A. F. (Org.), **Patterns of Change in Earth Evolution**, Berlin, Heidelberg, Springer Berlin Heidelberg, 1984. p. 345–355. DOI: 10.1007/978-3-642-69317-5_20. Disponível em: http://link.springer.com/10.1007/978-3-642-69317-5_20. Acesso em: 20 set. 2024.

TUPINAMBÁ, M., HEILBRON, M., VALERIANO, C., *et al.* "Juvenile contribution of the Neoproterozoic Rio Negro Magmatic Arc (Ribeira Belt, Brazil): Implications for Western Gondwana amalgamation", **Gondwana Research**, v. 21, n. 2–3, p. 422–438, mar. 2012. DOI: 10.1016/j.gr.2011.05.012.

TUPINAMBÁ, M., PENHA, H., JUNHO, M., "Arc-related to post-collisional magmatism at Serra dos Órgãos region, Rio de Janeiro State, Brazil: products of Gondwana assembly, during the Brasiliano-Pan African Orogeny". [S.l: s.n.], 2003. p. 1–10.

VALERIANO, C.M., MENDES, J.C., TUPINAMBÁ, M., BONGIOLO, E., HEILBRON, M., Junho, M.do. C.B., 2016. Cambro-Ordovician post-collisional granites of the Ribeira belt, SE Brazil: A case of terminal magmatism of a hot orogen. **J. South Am. Earth Sci.** 68, 269–281. https://doi.org/10.1016/j.jsames.2015.12.014.

VALERIANO, C. M., ALMEIDA, J. C. H. D., HEILBRON, M. **Precambrian gneisses in Rio: from the Sugar Loaf to the Arpoador outcrops - Field Trip Guide**. [S.l.], 31st IGC, 2000. Disponível em: http://rgdoi.net/10.13140/2.1.2574.1125. Acesso em: 20 ago. 2024.

VALERIANO, C. M. "PROGRAMA GEOLOGIA DO BRASIL - PGB INTEGRAÇÃO, ATUALIZAÇÃO E DIFUSÃO DE DADOS DA GEOLOGIA DO BRASIL", 2012.

VALERIANO, C. M., RUBEM PORTO JUNIOR, MONICA HEILBRON, *et al.* **Geologia e recursos minerais da folha Baía de Guanabara SF. 23-ZB-IV**, 2012.

VALERIANO, C. M. *et al.* U-Pb LA-MC-ICPMS geochronology of Cambro-Ordovician post-collisional granites of the Ribeira belt, southeast Brazil: Terminal Brasiliano magmatism in central Gondwana supercontinent. **Journal of South American Earth Sciences**, v. 32, n. 4, p. 416-428, 2011.

VALERIANO, C. M., MAGALHÃES, A. C. "Geologia estrutural de area do Pão de Açucar e adjacências, Rio de Janeiro, Brasil", **Geologia estrutural de area do Pão de Açucar e adjacências, Rio de Janeiro, Brasil**, v. 56, n. 3, p. 295–301, 1984.

VALLADARES, C. S., MACHADO, N., HEILBRON, M., *et al.* "Sedimentary provenance in the central Ribeira belt based on laser-ablation ICPMS207Pb/206Pb zircon ages", **Gondwana Research**, Neoproterozoic – Early Paleozoic events in Southwest Gondwana. v. 13, n. 4, p.

516–526, 1 jul. 2008. DOI: 10.1016/j.gr.2007.05.013.

VERMEESCH, P. "How many grains are needed for a provenance study?", **Earth and Planetary Science Letters**, v. 224, n. 3–4, p. 441–451, ago. 2004. DOI: 10.1016/j.epsl.2004.05.037.

VIEIRA, T. A. T., SCHMITT, R. da S., MENDES, J. C., *et al.* "Contrasting *P-T*-t paths of basement and cover within the Búzios Orogen, SE Brazil – Tracking Ediacaran-Cambrian subduction zones", **Precambrian Research**, v. 368, p. 106479, 1 jan. 2022. DOI: 10.1016/j.precamres.2021.106479.

WILLIAMS, I. S., CLAESSON, S. "Isotopic evidence for the Precambrian provenance and Caledonian metamorphism of high grade paragneisses from the Seve Nappes, Scandinavian Caledonides", **Contributions to Mineralogy and Petrology**, v. 97, n. 2, p. 205–217, 1 out. 1987. DOI: 10.1007/BF00371240.

ZHENG, Y., WU, Y., ZHAO, Z., *et al.* "Metamorphic effect on zircon Lu–Hf and U–Pb isotope systems in ultrahigh-pressure eclogite-facies metagranite and metabasite", **Earth and Planetary Science Letters**, v. 240, n. 2, p. 378–400, 1 dez. 2005. DOI: 10.1016/j.epsl.2005.09.025.

APENDICE A

Dados in situ de zircão U-Pb da amostra CC_05A obtidos por LA-MC-ICP-MS (Dados para o gráfico de Wetherill c).

			Isotope ratios[c]							Ages (Ma)						
Spot number	f_{206c}	Th/U[b]	$^{207}Pb/^{235}U$	2 s [%]	$^{206}Pb/^{238}U$	2 s [%]	RHO	$^{207}Pb/^{206}Pb$[e]	2 s [%]	$^{206}Pb/^{238}U$	2 s [abs]	$^{207}Pb/^{235}U$	2 s [abs]	$^{207}Pb/^{206}Pb$	2 s [abs]	% Conc[f]
CC_5A_III_29	0.76	0.92	0.600	4.092	0.072	2.483	0.607	0.060	3.253	449.877	10.798	477.329	15.705	611.487	70.288	94.2
CC_5A_III_36	1.35	1.78	0.708	6.010	0.085	3.467	0.577	0.061	4.910	523.343	17.450	543.496	25.615	628.935	105.784	96.3
CC_5A_III_30	3.03	0.56	0.740	12.846	0.086	7.201	0.561	0.062	10.638	534.033	37.013	562.398	57.046	678.873	227.320	95.0
CC_5A_III_31	1.58	0.40	0.740	8.194	0.088	3.975	0.485	0.061	7.165	544.409	20.787	562.161	36.004	634.678	154.233	96.8
CC_5A_III_38	2.34	1.16	0.737	9.773	0.089	5.432	0.556	0.060	8.124	549.383	28.672	560.624	43.002	606.515	175.709	98.0
CC_5A_II_51	4.84	0.19	0.742	20.801	0.090	10.970	0.527	0.060	17.674	554.591	58.562	563.369	94.177	598.978	382.712	98.4
CC_5A_I_10	0.76	0.43	0.840	3.828	0.091	1.809	0.473	0.067	3.374	563.103	9.763	619.322	17.906	830.540	70.342	90.9
CC_5A_III_14	4.09	0.20	0.814	10.932	0.092	4.420	0.404	0.062	14.412	565.170	49.410	585.691	78.831	666.061	308.614	96.5
CC_5A_I_44	1.89	0.75	0.819	7.889	0.092	4.240	0.537	0.064	6.653	569.420	23.150	607.287	36.713	751.228	140.489	93.8
CC_5A_II_53	2.10	0.12	0.783	9.792	0.092	4.846	0.495	0.061	8.509	570.070	26.492	587.198	44.628	653.981	182.571	97.1
CC_5A_II_09	1.80	0.13	0.802	7.714	0.093	4.044	0.524	0.063	6.569	571.722	22.164	598.092	35.479	699.391	139.901	95.6
CC_5A_II_04	1.43	0.11	0.792	6.705	0.095	3.227	0.481	0.061	5.877	583.333	18.022	592.402	30.547	627.292	126.663	98.5
CC_5A_I_37	1.23	0.10	0.823	5.628	0.096	2.780	0.494	0.062	4.893	591.160	15.724	609.708	26.130	679.238	104.548	97.0
CC_5A_I_45	1.21	0.66	0.847	5.393	0.096	2.744	0.509	0.064	4.643	591.219	15.519	623.142	25.431	740.834	98.210	94.9
CC_5A_I_04	0.31	0.40	0.833	2.537	0.096	0.892	0.352	0.063	2.375	591.983	5.048	615.293	11.775	702.033	50.560	96.2
CC_5A_I_42	2.37	0.26	0.796	10.256	0.097	5.035	0.491	0.060	8.935	596.510	28.751	594.838	47.251	588.467	193.818	100.3
CC_5A_I_01	0.39	0.64	0.874	2.840	0.099	1.035	0.365	0.064	2.644	608.780	6.016	637.848	13.539	742.221	55.923	95.4
CC_5A_III_25	0.67	0.18	0.833	4.001	0.099	1.853	0.463	0.061	3.546	609.015	10.777	615.158	18.630	637.832	76.293	99.0
CC_5A_I_34	1.68	0.15	0.822	7.488	0.099	3.556	0.475	0.060	6.590	611.185	20.767	609.379	34.904	602.672	142.614	100.3
CC_5A_III_33	2.42	1.36	0.912	9.198	0.100	5.037	0.548	0.066	7.696	613.647	29.552	657.961	45.546	812.985	160.916	93.3
CC_5A_II_28	0.66	0.18	0.841	4.297	0.101	1.859	0.433	0.060	3.874	619.798	10.994	619.938	20.134	620.450	83.583	100.0
CC_5A_II_27	1.27	0.17	0.931	6.535	0.101	2.984	0.457	0.067	5.814	620.325	17.672	668.176	32.507	833.087	121.173	92.8
CC_5A_II_50	3.20	0.75	0.841	13.524	0.101	6.558	0.485	0.060	11.828	621.672	38.984	619.756	64.757	612.767	255.531	100.3
CC_5A_II_29	2.97	0.51	0.802	12.835	0.101	6.081	0.474	0.057	11.303	621.964	36.158	598.228	59.747	509.243	248.516	104.0
CC_5A_II_42	0.41	0.58	0.824	3.471	0.101	1.520	0.438	0.059	3.121	622.784	9.031	610.007	16.044	562.841	67.993	102.1
CC_5A_III_42	1.34	3.21	0.881	5.626	0.102	2.955	0.525	0.063	4.787	624.539	17.615	641.500	27.112	701.688	101.906	97.4
CC_5A_II_54	0.58	0.28	0.879	4.086	0.102	1.767	0.432	0.063	3.685	624.773	10.528	640.477	19.598	696.268	78.510	97.5
CC_5A_II_26	1.28	0.74	0.947	6.217	0.104	2.865	0.461	0.066	5.518	637.983	17.427	676.573	31.179	807.222	115.474	94.3
CC_5A_II_45	4.14	1.38	0.885	16.480	0.105	8.044	0.488	0.061	14.383	644.344	49.516	643.425	81.745	640.199	309.332	100.1
CC_5A_II_46	0.97	0.98	0.894	4.994	0.105	2.282	0.457	0.062	4.442	646.269	14.051	648.661	24.224	656.994	95.255	99.6
CC_5A_II_49	0.99	1.81	0.840	5.124	0.106	2.310	0.451	0.058	4.574	647.202	14.238	619.113	24.034	517.713	100.422	104.5
CC_5A_III_41	0.61	312.80	0.859	3.665	0.106	1.784	0.487	0.059	3.202	647.960	11.005	629.500	17.342	563.735	69.744	102.9
CC_5A_II_47	2.55	2.05	0.794	11.577	0.106	5.049	0.436	0.054	10.418	652.040	31.386	593.299	53.396	374.605	234.467	109.9
CC_5A_I_39	2.22	0.65	0.893	9.257	0.106	4.337	0.469	0.061	8.179	652.273	26.962	648.080	45.345	633.504	176.087	100.6
CC_5A_III_19	0.71	1.86	0.922	4.256	0.107	1.885	0.443	0.062	3.815	658.038	11.804	663.663	20.948	682.819	81.474	99.2
CC_5A_III_05	4.83	0.63	1.116	11.828	0.108	4.848	0.410	0.071	14.922	662.867	57.701	734.906	95.845	961.259	304.836	90.2
CC_5A_II_02	0.53	0.17	0.965	3.141	0.109	1.390	0.443	0.065	2.816	664.147	8.780	685.998	15.784	758.344	59.402	96.8
CC_5A_II_21	0.61	0.69	0.909	3.759	0.109	1.657	0.441	0.061	3.374	665.135	10.480	656.607	18.342	627.416	72.724	101.3
CC_5A_II_07	0.73	0.31	0.964	3.662	0.109	1.675	0.457	0.064	3.256	666.356	10.614	685.193	18.414	747.553	68.811	97.3
CC_5A_III_16	0.71	1.60	0.922	3.861	0.110	1.779	0.461	0.061	3.426	674.548	11.402	663.245	18.977	625.009	73.873	101.7
CC_5A_II_03	1.15	0.44	0.973	5.001	0.112	2.315	0.463	0.063	4.433	683.889	15.036	690.101	25.356	710.402	94.233	99.1
CC_5A_I_32	0.86	0.66	0.901	4.172	0.113	1.829	0.438	0.058	3.750	687.772	11.943	652.249	20.281	531.196	82.142	105.4
CC_5A_II_43	1.43	0.80	0.962	6.553	0.116	2.837	0.433	0.060	5.907	707.153	19.028	684.098	33.151	608.979	127.694	103.4
CC_5A_III_10	2.86	0.12	1.089	8.278	0.118	3.912	0.473	0.065	9.747	716.735	34.753	732.832	59.137	782.371	204.812	97.8
CC_5A_III_28	4.94	0.55	1.171	17.723	0.121	8.427	0.476	0.070	15.591	737.812	59.022	787.250	102.037	930.001	320.060	93.7
CC_5A_III_26	4.43	0.37	1.219	15.210	0.123	7.437	0.489	0.072	13.267	745.856	52.597	809.098	88.577	987.326	269.956	92.2
CC_5A_II_31	2.23	0.74	1.060	9.175	0.123	3.960	0.432	0.063	8.277	745.971	27.953	733.613	49.096	696.051	176.365	101.7
CC_5A_III_03	2.75	0.33	1.139	8.618	0.123	4.034	0.468	0.065	9.495	746.200	33.636	757.030	58.321	789.155	199.284	98.6
CC_5A_III_23	3.98	1.02	1.180	14.284	0.124	6.678	0.467	0.069	12.627	751.825	47.562	791.321	81.707	904.285	260.243	95.0
CC_5A_II_17	0.74	0.49	1.173	3.811	0.124	1.789	0.469	0.069	3.365	753.259	12.733	787.856	21.106	887.088	69.548	95.6
CC_5A_III_27	2.90	0.33	1.198	10.767	0.125	4.940	0.459	0.070	9.566	759.221	35.481	799.632	61.403	913.956	196.866	94.9
CC_5A_II_35	2.01	1.26	1.167	8.087	0.125	3.580	0.443	0.068	7.251	760.539	25.733	785.167	45.208	855.795	150.589	96.9
CC_5A_I_40	0.60	0.91	1.271	9.983	0.125	3.227	0.323	0.074	9.447	761.283	23.212	832.711	58.373	1028.402	191.035	91.4
CC_5A_II_22	2.11	1.48	1.135	8.394	0.127	3.647	0.434	0.065	7.561	768.726	26.483	770.158	46.355	774.313	159.071	99.8
CC_5A_III_07	0.92	1.18	1.228	6.065	0.127	3.414	0.563	0.069	4.045	773.016	14.466	808.381	25.426	907.068	83.331	95.6
CC_5A_II_56	3.43	1.63	1.147	12.643	0.128	5.595	0.442	0.065	11.338	775.817	41.024	776.016	71.021	776.587	238.459	100.0
CC_5A_II_15	0.52	0.48	1.129	3.212	0.129	1.437	0.447	0.064	2.873	779.474	10.559	767.418	17.447	732.480	60.850	101.6
CC_5A_II_55	0.59	1.01	1.172	3.544	0.129	1.587	0.448	0.066	3.169	783.471	11.722	787.623	19.606	799.398	66.398	99.5
CC_5A_II_05	2.24	0.33	1.227	8.290	0.130	3.650	0.440	0.069	7.443	786.439	27.081	812.855	47.464	885.885	153.843	96.8
CC_5A_II_38	1.91	1.24	1.165	8.189	0.131	3.353	0.410	0.065	7.471	792.314	25.050	784.317	45.758	761.637	157.500	101.0
CC_5A_III_18	3.60	0.80	1.172	13.306	0.131	5.716	0.430	0.065	12.016	794.480	42.869	787.380	75.640	767.320	253.092	100.9
CC_5A_II_11	0.40	0.60	1.230	2.785	0.132	1.159	0.416	0.068	2.532	796.930	8.697	814.387	15.720	862.393	52.539	97.9
CC_5A_I_41	2.29	0.73	1.248	8.741	0.134	3.637	0.416	0.067	7.948	811.497	27.790	822.415	50.504	852.051	165.169	98.7
CC_5A_III_09	0.89	1.37	1.289	5.705	0.136	3.310	0.580	0.068	3.883	821.833	14.367	835.550	24.820	872.194	80.437	98.4
CC_5A_I_35	2.27	0.74	1.247	8.574	0.137	3.531	0.412	0.066	7.814	825.634	27.419	821.920	49.498	811.885	163.406	100.5
CC_5A_II_33	1.33	0.21	1.466	5.519	0.142	2.374	0.430	0.075	4.982	856.244	19.066	916.586	33.877	1064.822	100.198	93.4
CC_5A_II_44	4.51	1.47	1.350	15.939	0.143	6.594	0.414	0.069	14.511	860.646	53.343	867.681	97.517	885.690	299.951	99.2
CC_5A_II_48	2.23	1.90	1.344	8.534	0.143	3.494	0.409	0.068	7.786	863.240	28.295	864.980	50.942	869.440	161.345	99.8
CC_5A_III_02	1.99	0.42	1.383	7.050	0.145	3.692	0.524	0.068	6.875	872.311	25.475	869.991	45.096	864.087	142.599	100.3
CC_5A_II_18	2.10	0.56	1.517	7.867	0.145	3.324	0.423	0.076	7.130	872.931	27.197	937.289	49.324	1091.790	142.815	93.1
CC_5A_III_01	5.54	0.96	1.738	10.640	0.148	4.876	0.458	0.081	14.853	887.833	64.632	986.250	111.638	1212.228	292.291	90.0
CC_5A_II_34	1.04	2.07	1.421	4.712	0.148	1.958	0.415	0.070	4.286	890.079	16.295	897.711	28.478	916.548	88.175	99.1
CC_5A_II_30	2.20	1.36	1.350	8.653	0.152	3.302	0.382	0.065	7.999	910.094	28.088	867.764	51.782	761.179	168.643	104.9
CC_5A_II_39	1.99	1.43	1.504	7.554	0.157	2.966	0.393	0.069	6.947	940.808	26.017	932.210	47.154	911.938	143.015	100.9
CC_5A_II_19	0.97	1.25	1.502	4.670	0.158	1.845	0.395	0.069	4.290	943.091	16.212	931.310	28.878	903.529	88.438	101.3
CC_5A_III_43	5.84	1.01	1.582	18.002	0.158	7.559	0.420	0.073	16.338	944.985	66.788	963.248	118.677	1005.170	331.545	98.1
CC_5A_I_38	3.61	1.83	1.536	12.658	0.161	4.711	0.372	0.069	11.748	960.888	42.191	945.085	81.000	908.448	241.981	101.7

CC_5A_II_20	1.11	1.91	1.486	4.852	0.161	1.901	0.392	0.067	4.465	963.775	17.038	924.585	29.885	832.234	93.067	104.2
CC_5A_III_53	4.42	0.61	1.677	13.368	0.162	5.683	0.425	0.075	12.100	966.772	51.228	1000.031	88.815	1073.679	243.007	96.7
CC_5A_I_36	1.29	1.45	1.577	5.077	0.163	1.936	0.381	0.070	4.693	970.988	17.472	961.202	32.046	938.882	96.212	101.0
CC_5A_III_21	1.86	1.20	1.815	6.374	0.166	2.743	0.430	0.079	5.753	988.652	25.189	1050.903	42.609	1182.644	113.702	94.1
CC_5A_II_06	1.76	0.92	1.868	5.734	0.168	2.378	0.415	0.080	5.217	1003.290	22.129	1069.867	38.645	1208.206	102.729	93.8
CC_5A_II_37	1.57	3.07	1.742	6.162	0.176	2.340	0.380	0.072	5.700	1043.660	22.583	1024.326	40.548	983.250	116.056	101.9
CC_5A_III_20	1.70	1.10	1.804	5.940	0.177	2.359	0.397	0.074	5.451	1051.988	22.934	1046.941	39.563	1036.423	110.097	100.5
CC_5A_III_52	5.53	1.37	2.379	13.862	0.189	6.058	0.437	0.091	12.468	1117.148	62.439	1236.346	104.272	1450.578	237.303	90.4
CC_5A_II_41	1.12	1.77	3.205	3.776	0.254	1.587	0.420	0.092	3.427	1456.758	20.723	1458.473	29.654	1460.974	65.128	99.9
CC_5A_III_22	5.31	2.64	3.216	14.155	0.249	4.868	0.344	0.094	13.292	1433.317	62.861	1461.050	116.023	1501.604	251.259	98.1
CC_5A_II_10	1.50	0.42	4.204	4.095	0.267	1.623	0.396	0.114	3.760	1523.877	22.065	1674.814	34.162	1869.492	67.834	91.0
CC_5A_III_13	0.22	1.24	5.170	4.547	0.308	3.002	0.660	0.121	2.302	1731.547	18.390	1845.761	22.364	1977.054	41.009	93.8

APENDICE B

Dados in situ de zircão U-Pb da amostra CC_03B obtidos por LA-MC-ICP-MS (Dados para o gráfico de Wetherill c).

			Isotope ratios[c]							Ages (Ma)						
Spot number	f_{206c}	Th/U[b]	$^{207}Pb/^{235}U$	2 s [%]	$^{206}Pb/^{238}U$	2 s [%]	RHO	$^{207}Pb/^{206}Pb$[e]	2 s [%]	$^{206}Pb/^{238}U$	2 s [abs]	$^{207}Pb/^{235}U$	2 s [abs]	$^{207}Pb/^{206}Pb$	2 s [abs]	% Conc[f]
8_CC-3B	0.00	0.46	0.740	14.871	0.086	7.629	0.51	0.062	12.765	533.321	39.169	562.476	66.344	682.233	272.620	94.8
156_CC-3B	0.01	2.61	0.751	4.976	0.090	3.031	0.61	0.061	3.947	553.644	16.099	568.669	21.903	629.210	85.043	97.4
7_CC-3B	0.00	0.92	0.781	11.379	0.095	5.906	0.52	0.060	9.727	582.390	32.970	586.295	51.991	601.444	210.541	99.3
94_CC-3B	0.03	1.88	0.776	21.877	0.095	11.530	0.53	0.059	18.592	584.746	64.778	583.031	101.995	576.360	404.140	100.3
135_CC-3B	0.01	0.43	0.820	4.533	0.095	2.763	0.61	0.062	3.594	587.277	15.529	607.958	20.951	685.807	76.707	96.6
62_CC-3B	0.03	2.41	0.786	21.991	0.097	11.293	0.51	0.059	18.870	599.095	64.932	588.982	103.366	550.201	411.993	101.7
153_CC-3B	0.01	0.35	0.936	5.596	0.099	3.397	0.61	0.069	4.447	606.140	19.681	671.011	27.856	895.374	91.783	90.3
19_CC-3B	0.02	2.72	0.821	10.497	0.099	5.495	0.52	0.060	8.944	607.314	31.929	608.705	49.235	613.886	193.192	99.8
80_CC-3B	0.03	1.12	0.815	19.337	0.099	9.980	0.52	0.060	16.563	607.549	58.126	605.178	92.223	596.312	358.824	100.4
56_CC-3B	0.02	1.11	0.926	13.515	0.101	7.371	0.55	0.066	11.328	623.018	43.923	665.563	68.223	812.444	236.888	93.6
157_CC-3B	0.01	0.18	0.958	7.447	0.102	4.316	0.58	0.068	6.069	623.428	25.699	682.054	37.681	880.657	125.546	91.4
152_CC-3B	0.01	0.49	0.898	5.205	0.102	3.054	0.59	0.064	4.215	626.002	18.244	650.751	25.321	737.559	89.208	96.2
57_CC-3B	0.01	1.20	0.851	8.975	0.103	4.564	0.51	0.060	7.727	632.551	27.558	625.123	42.781	598.337	167.353	101.2
27_CC-3B	0.02	2.67	1.009	10.281	0.107	5.537	0.54	0.069	8.663	653.205	34.486	708.216	53.825	886.810	179.041	92.2
32_CC-3B	0.02	0.88	0.905	10.022	0.108	5.003	0.50	0.061	8.684	658.911	31.414	654.299	49.528	638.428	186.814	100.7
40_CC-3B	0.01	0.15	0.920	6.375	0.108	3.271	0.51	0.062	5.472	663.682	20.665	662.572	31.509	658.797	117.318	100.2
132_CC-3B	0.01	0.95	0.915	5.060	0.109	2.850	0.56	0.061	4.181	666.066	18.060	659.548	24.844	637.325	89.949	101.0
93_CC-3B	0.04	1.03	0.907	22.901	0.109	11.028	0.48	0.060	20.071	666.996	70.257	655.522	117.104	616.232	433.378	101.8
42_CC-3B	0.02	2.37	0.918	11.530	0.110	5.597	0.49	0.061	10.080	671.702	35.801	661.124	57.626	625.206	217.323	101.6
15_CC-3B	0.03	1.82	0.940	15.707	0.111	7.669	0.49	0.062	13.708	676.348	49.431	672.629	80.355	660.195	293.826	100.6
139_CC-3B	0.01	0.60	0.964	5.096	0.112	2.865	0.56	0.063	4.214	683.251	18.600	685.322	25.717	692.129	89.849	99.7
10_CC-3B	0.01	1.88	0.954	8.199	0.112	4.074	0.50	0.062	7.116	683.425	26.471	680.044	41.477	668.867	152.302	100.5
147_CC-3B	0.01	0.68	1.042	7.498	0.112	4.065	0.54	0.067	6.300	686.845	26.537	724.930	39.611	844.601	131.074	94.7
155_CC-3B	0.01	1.08	1.001	8.162	0.114	4.223	0.52	0.064	6.984	695.473	27.904	704.529	42.338	733.508	147.923	98.7
158_CC-3B	0.01	1.76	1.081	5.372	0.116	3.056	0.57	0.068	4.418	705.593	20.460	744.137	28.737	861.903	91.655	94.8
37_CC-3B	0.01	0.40	1.145	4.023	0.123	2.189	0.54	0.068	3.376	745.913	15.438	774.683	22.040	858.525	70.072	96.3
133_CC-3B	0.01	1.16	1.243	5.359	0.123	3.082	0.58	0.073	4.384	749.357	21.840	820.036	30.608	1016.899	88.810	91.4
43_CC-3B	0.03	0.79	1.044	17.088	0.125	7.530	0.44	0.061	15.340	756.527	53.977	725.705	92.713	631.613	330.365	104.2
29_CC-3B	0.03	1.58	1.099	18.828	0.125	8.515	0.45	0.064	16.792	762.028	61.489	752.926	105.384	725.978	356.073	101.2
130_CC-3B	0.00	1.03	1.244	3.746	0.126	2.377	0.63	0.072	2.896	763.574	17.136	820.634	21.309	978.591	59.007	93.0
49_CC-3B	0.02	1.53	1.083	12.765	0.126	5.754	0.45	0.062	11.394	763.574	41.566	745.046	69.724	689.775	243.046	102.5
12_CC-3B	0.03	1.89	1.107	16.855	0.128	7.371	0.44	0.063	15.157	776.960	54.179	756.504	94.128	696.500	322.961	102.7
20_CC-3B	0.01	1.70	1.114	7.988	0.129	3.683	0.46	0.063	7.089	780.045	27.118	760.144	43.671	702.052	150.901	102.6
129_CC-3B	0.04	1.13	1.179	20.310	0.129	9.390	0.46	0.066	18.009	780.902	69.430	790.623	118.178	818.137	376.246	98.8
50_CC-3B	0.04	1.14	1.372	19.505	0.142	8.662	0.44	0.070	17.477	853.704	69.632	877.093	121.558	936.599	358.397	97.3
18_CC-3B	0.02	0.45	1.304	11.913	0.144	5.099	0.43	0.066	10.767	864.424	41.385	847.568	70.884	803.686	225.459	102.0
16_CC-3B	0.01	2.32	1.364	7.337	0.145	3.292	0.45	0.068	6.558	873.831	26.957	873.633	43.926	873.132	135.816	100.0
11_CC-3B	0.02	1.74	1.321	12.094	0.147	4.986	0.41	0.065	11.019	882.326	41.245	855.123	72.425	785.213	231.423	103.2
48_CC-3B	0.04	1.41	1.365	18.840	0.149	7.728	0.41	0.066	17.181	895.187	64.921	873.933	116.878	820.455	358.827	102.4
63_CC-3B	0.02	2.01	1.529	12.352	0.161	4.985	0.40	0.069	11.301	960.388	44.631	941.994	78.801	899.234	233.109	102.0
35_CC-3B	0.02	5.05	1.612	11.702	0.163	4.855	0.41	0.072	10.648	972.817	43.987	974.992	76.119	979.894	216.900	99.8
33_CC-3B	0.03	1.37	1.624	16.606	0.166	6.594	0.40	0.071	15.241	991.472	60.887	979.703	110.129	953.417	311.733	101.2
61_CC-3B	0.02	1.03	2.351	7.443	0.203	3.093	0.42	0.084	6.770	1192.541	33.762	1227.833	54.457	1290.357	131.749	97.1
46_CC-3B	0.01	0.72	2.553	8.164	0.216	3.083	0.38	0.086	7.560	1262.984	35.458	1287.270	61.384	1328.023	146.335	98.1
9_CC-3B	0.02	1.81	3.108	10.373	0.250	3.768	0.36	0.090	9.665	1438.785	48.775	1434.693	82.990	1428.629	184.498	100.3
59_CC-3B	0.03	2.91	3.125	12.299	0.224	5.192	0.42	0.101	11.149	1302.502	61.528	1438.769	99.304	1646.414	206.788	90.5
45_CC-3B	0.03	2.64	4.126	8.903	0.278	3.477	0.39	0.108	8.196	1580.677	48.924	1659.533	75.500	1760.824	149.827	95.2
148_CC-3B	0.01	4.32	5.657	3.730	0.330	2.222	0.60	0.124	2.996	1838.382	35.647	1924.877	32.708	2019.353	53.100	95.5

APENDICE C

Dados in situ de zircão U-Pb da amostra Ni_01 obtidos por LA-MC-ICP-MS (Dados para o gráfico de Wetherill c).

			Isotope ratios[c]							Ages (Ma)						
Spot number	*f* 206c	Th/U[b]	$^{207}Pb/^{235}U$	2 s [%]	$^{206}Pb/^{238}U$	2 s [%]	RHO	$^{207}Pb/^{206}Pb$[e]	2 s [%]	$^{206}Pb/^{238}U$	2 s [abs]	$^{207}Pb/^{235}U$	2 s [abs]	$^{207}Pb/^{206}Pb$	2 s [abs]	% Conc[f]
NI_01_042	4.63	0.03	0.707	4.043	0.085	2.413	0.597	0.060	4.042	525.720	12.192	543.127	17.149	616.862	87.261	96.8
NI_01_075	4.67	0.02	0.681	4.004	0.085	2.462	0.615	0.058	4.003	527.621	12.486	527.668	16.614	527.872	87.741	100.0
NI_01_059	4.70	0.03	0.754	3.977	0.088	2.452	0.616	0.062	3.976	541.861	12.755	570.599	17.512	686.820	84.858	95.0
NI_01_104	4.41	0.09	0.707	4.243	0.088	3.535	0.833	0.058	4.242	541.920	18.399	542.905	18.002	547.044	92.671	99.8
NI_01_064	4.67	0.04	0.725	4.004	0.088	2.451	0.612	0.060	4.003	541.979	12.755	553.616	17.234	601.770	86.650	97.9
NI_01_071	4.68	0.03	0.717	3.995	0.088	2.500	0.626	0.059	3.994	543.757	13.048	548.922	17.082	570.414	86.903	99.1
NI_01_076	4.71	0.03	0.710	3.974	0.088	0.997	0.251	0.058	3.973	545.120	5.215	544.986	16.901	544.426	86.835	100.1
NI_01_061	4.62	0.05	0.756	4.045	0.089	1.006	0.249	0.061	4.044	552.284	5.328	571.863	17.844	650.478	86.830	96.6
NI_01_027	4.62	0.03	0.734	4.047	0.090	2.396	0.592	0.059	4.046	553.940	12.731	558.843	17.543	578.860	87.908	99.1
NI_01_018	4.52	0.06	0.777	4.142	0.090	2.450	0.591	0.063	4.141	554.295	13.027	583.903	18.563	700.787	88.180	94.9
NI_01_113	4.50	0.02	0.717	4.154	0.090	3.502	0.843	0.058	4.153	555.182	18.658	548.687	17.763	521.809	91.112	101.2
NI_01_087	4.66	0.06	0.732	4.017	0.090	2.490	0.620	0.059	4.016	557.725	13.316	557.821	17.390	558.215	87.571	100.0
NI_01_021	4.64	0.09	0.841	4.033	0.090	2.434	0.603	0.067	4.032	557.843	13.020	619.561	18.878	852.008	83.787	90.2
NI_01_058	4.58	0.05	0.733	4.080	0.090	2.434	0.596	0.059	4.079	557.902	13.019	558.548	17.680	561.181	88.890	99.9
NI_01_110	4.42	0.03	0.730	4.233	0.090	3.539	0.836	0.059	4.232	557.961	18.946	556.842	18.308	552.267	92.368	100.2
NI_01_074	4.66	0.04	0.739	3.996	0.091	2.479	0.620	0.059	3.995	560.089	13.311	562.060	17.394	570.045	86.923	99.6
NI_01_049	4.68	0.06	0.737	4.011	0.091	2.424	0.604	0.059	4.010	560.089	13.015	560.378	17.424	561.551	87.388	99.9
NI_01_077	4.66	0.09	0.741	4.068	0.091	2.472	0.608	0.059	4.067	561.626	13.308	562.783	17.730	567.465	88.540	99.8
NI_01_037	4.60	0.03	0.738	4.015	0.091	2.417	0.602	0.059	4.014	561.626	13.012	561.245	17.459	559.699	87.490	100.1
NI_01_114	3.95	0.09	0.744	4.732	0.091	3.619	0.765	0.059	4.731	562.571	19.525	564.787	20.710	573.724	102.891	99.6
NI_01_068	4.67	0.04	0.743	4.006	0.092	2.458	0.614	0.059	4.005	564.520	13.302	564.445	17.498	564.141	87.246	100.0
NI_01_070	4.67	0.04	0.744	4.008	0.092	2.457	0.613	0.059	4.007	564.816	13.301	564.534	17.506	563.402	87.286	100.0
NI_01_063	4.68	0.07	0.748	3.998	0.092	2.448	0.612	0.059	3.997	566.823	13.297	567.172	17.526	568.571	87.003	99.9
NI_01_048	4.60	0.07	0.748	4.069	0.092	2.446	0.601	0.059	4.068	567.237	13.296	567.208	17.838	567.096	88.560	100.0
NI_01_002	4.72	0.01	0.744	3.959	0.092	2.334	0.590	0.059	3.958	567.945	12.703	564.896	17.301	552.640	86.389	100.6
NI_01_041	4.63	0.08	0.755	4.041	0.092	2.441	0.604	0.059	4.040	568.476	13.294	571.146	17.810	581.788	87.746	99.5
NI_01_079	4.66	0.10	0.760	4.018	0.092	2.494	0.621	0.060	4.017	568.594	13.589	573.812	17.766	594.533	87.045	99.1
NI_01_073	4.67	0.06	0.751	4.003	0.092	2.490	0.622	0.059	4.002	569.479	13.587	568.781	17.584	565.989	87.145	100.1
NI_01_066	4.69	0.07	0.755	3.985	0.092	2.488	0.624	0.059	3.984	570.070	13.586	571.245	17.560	575.928	86.602	99.8
NI_01_045	4.68	0.09	0.753	3.997	0.092	2.433	0.609	0.059	3.996	570.188	13.290	570.011	17.586	569.309	86.963	100.0
NI_01_034	4.57	0.22	0.760	4.097	0.093	2.431	0.593	0.060	4.096	570.719	13.289	574.197	18.129	587.991	88.861	99.4
NI_01_098	4.17	0.09	0.765	4.489	0.093	3.551	0.791	0.060	4.488	572.901	19.494	576.981	19.954	593.082	97.290	99.3
NI_01_047	4.68	0.11	0.757	3.996	0.093	2.421	0.606	0.059	3.995	572.960	13.285	572.300	17.636	569.677	86.943	100.1
NI_01_014	4.67	0.04	0.757	4.004	0.093	2.364	0.590	0.059	4.003	573.668	12.988	572.049	17.663	565.619	87.165	100.3
NI_01_084	4.66	0.07	0.755	4.013	0.093	2.470	0.616	0.059	4.012	573.904	13.578	571.272	17.684	560.811	87.429	100.5
NI_01_067	4.62	0.11	0.762	4.052	0.093	2.467	0.609	0.059	4.051	574.553	13.577	574.904	17.943	576.294	88.050	100.0
NI_01_120	4.32	0.07	0.761	4.330	0.093	3.535	0.816	0.059	4.329	575.378	19.486	574.673	19.184	571.886	94.180	100.1
NI_01_020	4.69	0.05	0.765	3.991	0.094	2.399	0.601	0.059	3.990	577.972	13.274	576.888	17.718	572.621	86.782	100.2
NI_01_040	4.59	0.09	0.829	4.074	0.094	2.443	0.600	0.064	4.073	579.975	13.565	612.860	18.919	736.334	86.215	94.7
NI_01_026	4.63	0.09	0.771	4.044	0.094	2.390	0.591	0.059	4.042	580.034	13.270	580.168	18.030	580.691	87.807	100.0
NI_01_106	4.34	0.14	0.795	4.311	0.094	1.423	0.330	0.061	4.310	580.270	7.899	594.258	19.582	648.025	92.575	97.6
NI_01_115	4.26	0.11	0.770	4.387	0.094	3.555	0.810	0.059	4.386	580.506	19.766	579.873	19.568	577.395	95.321	100.1
NI_01_117	4.26	0.08	0.769	4.392	0.094	3.554	0.809	0.059	4.391	580.623	19.766	579.445	19.581	574.826	95.475	100.2
NI_01_004	4.70	0.03	0.771	3.982	0.094	2.333	0.586	0.059	3.980	580.800	12.973	580.182	17.751	577.761	86.502	100.1
NI_01_100	4.35	0.07	0.777	4.301	0.095	3.538	0.823	0.060	4.300	583.215	19.758	583.968	19.281	586.898	93.296	99.9
NI_01_017	4.63	0.03	0.777	4.037	0.095	2.426	0.601	0.059	4.036	583.922	13.557	584.008	18.088	584.345	87.605	100.0
NI_01_011	4.66	0.07	0.781	4.018	0.095	2.320	0.577	0.060	4.017	583.980	12.967	586.144	18.052	594.533	87.045	99.6
NI_01_032	4.63	0.25	0.792	4.040	0.095	2.420	0.599	0.060	4.038	585.335	13.554	592.212	18.289	618.649	87.162	98.9
NI_01_054	4.64	0.07	0.784	4.027	0.095	2.412	0.599	0.060	4.025	587.100	13.550	587.658	18.126	589.811	87.304	99.9
NI_01_015	4.70	0.06	0.782	3.979	0.096	2.354	0.592	0.059	3.978	588.395	13.253	586.511	17.883	579.227	86.423	100.3
NI_01_118	4.29	0.08	0.786	4.363	0.096	3.557	0.815	0.060	4.362	588.513	20.037	588.630	19.681	589.083	94.623	100.0
NI_01_003	4.64	0.05	0.787	4.029	0.096	2.349	0.583	0.060	4.028	589.689	13.250	589.489	18.177	588.719	87.364	100.1
NI_01_089	4.71	0.09	0.891	3.974	0.096	2.453	0.617	0.067	3.973	589.807	13.839	646.924	19.196	851.700	82.571	91.3
NI_01_025	4.65	0.05	0.791	4.026	0.096	2.391	0.594	0.060	4.025	592.160	13.540	591.749	18.217	590.175	87.284	100.1
NI_01_053	4.66	0.07	0.795	4.013	0.096	2.438	0.608	0.060	4.011	593.218	13.832	594.092	18.209	597.432	86.887	99.9
NI_01_080	4.66	0.07	0.795	4.013	0.096	2.489	0.620	0.060	4.012	593.395	14.126	594.157	18.214	597.070	86.907	99.9
NI_01_094	4.30	0.08	0.796	4.351	0.097	3.521	0.809	0.060	4.350	594.159	20.019	594.387	19.768	595.258	94.256	100.0
NI_01_057	4.66	0.12	0.863	4.015	0.097	2.433	0.606	0.065	4.014	594.335	13.830	631.563	19.057	767.199	84.540	94.1
NI_01_108	4.44	0.06	0.801	4.215	0.097	3.500	0.830	0.060	4.214	597.685	20.008	597.406	19.216	596.346	91.294	100.1
NI_01_107	4.35	0.10	0.799	4.300	0.097	3.544	0.824	0.060	4.299	598.860	20.299	596.443	19.584	587.263	93.274	100.4
NI_01_051	4.67	0.12	0.809	4.005	0.098	2.452	0.612	0.060	4.003	601.855	14.108	601.838	18.348	601.770	86.650	100.0
NI_01_096	4.26	0.08	0.819	4.391	0.099	3.545	0.807	0.060	4.390	606.962	20.568	607.311	20.271	608.615	94.905	99.9
NI_01_078	4.73	0.20	0.946	3.956	0.100	2.455	0.621	0.069	3.955	613.178	14.377	676.199	19.720	892.149	81.661	90.7
NI_01_102	4.21	0.10	0.834	4.440	0.100	3.542	0.798	0.060	4.439	615.757	20.834	615.993	20.717	616.862	95.844	100.0
NI_01_001	4.63	0.08	0.841	4.040	0.101	0.931	0.231	0.060	4.038	619.857	5.506	619.597	18.911	618.649	87.162	100.1
NI_01_097	4.46	0.06	0.887	4.194	0.102	3.524	0.840	0.063	4.193	626.996	21.091	644.625	20.216	706.880	89.192	97.3
NI_01_101	4.40	0.23	0.877	4.248	0.102	3.520	0.829	0.062	4.246	627.698	21.088	639.176	20.350	679.962	90.725	98.3

NI_01_109	4.42	0.15	0.859	4.235	0.103	3.543	0.837	0.060	4.234	632.025	21.367	629.498	20.064	620.434	91.346	100.4
NI_01_116	4.41	0.28	0.988	4.245	0.104	3.551	0.836	0.069	4.244	638.917	21.637	697.884	21.657	892.749	87.632	91.6
NI_01_099	4.26	0.11	0.880	4.394	0.105	3.535	0.805	0.061	4.393	641.661	21.628	641.202	21.107	639.587	94.480	100.1
NI_01_013	4.68	0.04	1.067	3.998	0.109	2.343	0.586	0.071	3.996	666.066	14.842	737.089	21.169	959.427	81.659	90.4
NI_01_085	4.73	0.32	1.073	3.955	0.110	2.457	0.621	0.071	3.954	672.167	15.701	740.278	21.004	952.222	80.883	90.8
NI_01_105	4.12	0.06	0.913	4.535	0.110	3.578	0.789	0.060	4.533	675.070	22.973	658.820	22.221	603.575	98.092	102.5
NI_01_012	4.68	0.19	1.041	3.997	0.116	2.327	0.582	0.065	3.996	707.673	15.615	724.417	20.916	776.601	84.036	97.7
NI_01_062	4.71	0.42	1.310	3.974	0.131	2.481	0.624	0.073	3.972	793.625	18.551	850.037	23.144	1000.290	80.658	93.4
NI_01_050	4.73	0.30	1.344	3.954	0.134	2.431	0.615	0.073	3.952	808.939	18.507	864.751	23.281	1010.618	80.123	93.6
NI_01_019	4.64	0.29	1.377	4.028	0.140	2.400	0.596	0.072	4.025	842.230	18.978	879.117	23.971	973.168	82.080	95.8
NI_01_072	4.71	0.22	1.441	3.975	0.140	2.461	0.619	0.075	3.972	845.850	19.535	905.983	24.105	1055.584	79.991	93.4
NI_01_052	4.68	0.38	1.553	3.994	0.142	2.424	0.607	0.079	3.992	857.768	19.499	951.832	24.979	1176.139	78.968	90.2
NI_01_056	4.70	0.09	1.523	3.982	0.157	2.421	0.608	0.070	3.979	939.861	21.208	939.654	24.705	939.169	81.565	100.0
NI_01_022	4.58	0.12	1.617	4.082	0.159	2.445	0.599	0.074	4.079	953.942	21.719	976.983	25.941	1029.146	82.469	97.6
NI_01_043	4.59	1.44	1.966	4.075	0.186	2.445	0.600	0.077	4.070	1099.996	24.777	1104.067	27.803	1112.098	81.283	99.6
NI_01_092	4.39	1.20	2.007	4.264	0.189	3.543	0.831	0.077	4.260	1116.552	36.425	1118.039	29.322	1120.931	84.963	99.9
NI_01_044	4.63	1.15	2.266	4.040	0.205	2.443	0.605	0.080	4.034	1200.412	26.811	1201.913	28.866	1204.611	79.479	99.9
NI_01_035	4.67	1.05	3.021	4.003	0.243	2.426	0.606	0.090	3.995	1403.052	30.668	1412.933	31.002	1427.862	76.275	99.3
NI_01_111	4.51	1.02	3.393	4.143	0.262	3.508	0.847	0.094	4.135	1501.547	47.156	1502.853	33.027	1504.695	78.134	99.9

APENDICE D

Dados in situ de zircão Lu-Hf da amostra CC_05A obtidos por LA-MC-ICP-MS.

			Sample (Present day ratios)						Sample Initial Ratios		
Name	U/Pb Age (Ma)	±2s	$^{176}Hf/^{177}Hf$ (t)	±2SE	$^{176}Lu/^{177}Hf$	±2SE	CHUR $^{176}Hf/^{177}Hf$ (t)	DM $^{176}Hf/^{177}Hf$ (t)	$^{176}Hf/^{177}Hf$ (t)	εHf(t)	±2SE
CC_05A III_25	609	11	0.28201	0.00008	0.000786	4.07E-05	0.28240	0.28281	0.28200	-14.3	0.998
CC_05A II_28	620	11	0.28223	0.00008	0.000857	2.54E-05	0.28239	0.28280	0.28222	-6.1	0.289
CC_05A II_27	620	18	0.28193	0.00007	0.000716	1.28E-05	0.28239	0.28280	0.28193	-16.6	0.780
CC_05A II_42	623	9	0.28204	0.00007	0.000636	1.71E-05	0.28239	0.28280	0.28204	-12.6	0.524
CC_05A II_45	644	50	0.28219	0.00009	0.000944	5.89E-05	0.28238	0.28278	0.28218	-7.1	0.995
CC_05A II_46	646	14	0.28217	0.00007	0.001035	9.79E-05	0.28238	0.28278	0.28215	-7.9	0.921
CC_05A III_19	658	12	0.28199	0.00011	0.001132	2.20E-05	0.28237	0.28277	0.28197	-14.1	0.533
CC_05A II_21	665	10	0.28212	0.00011	0.000701	1.85E-05	0.28237	0.28277	0.28212	-8.8	0.376
CC_05A III_16	675	11	0.28232	0.00013	0.000698	5.59E-05	0.28236	0.28276	0.28231	-1.7	0.162
CC_05A II_31	746	28	0.28182	0.00008	0.000753	1.01E-05	0.28231	0.28271	0.28180	-18.0	0.922
CC_05A II_22	769	26	0.28243	0.00010	0.001460	6.11E-05	0.28230	0.28269	0.28241	4.0	0.307
CC_05A II_56	776	41	0.28228	0.00006	0.000341	6.28E-05	0.28229	0.28268	0.28227	-0.8	0.194
CC_05A II_15	779	11	0.28195	0.00009	0.000817	5.15E-05	0.28229	0.28268	0.28194	-12.6	0.969
CC_05A II_55	783	12	0.28198	0.00007	0.001020	4.05E-05	0.28229	0.28268	0.28196	-11.6	0.636
CC_05A II_38	792	25	0.28188	0.00006	0.000556	9.78E-06	0.28228	0.28267	0.28187	-14.6	0.720
CC_05A III_18	794	43	0.28238	0.00006	0.001036	2.04E-05	0.28228	0.28267	0.28237	2.9	0.218
CC_05A III_9	822	14	0.28200	0.00012	0.001021	2.90E-05	0.28227	0.28265	0.28199	-9.8	0.454
CC_05A II_44	861	53	0.28220	0.00008	0.000725	5.31E-05	0.28224	0.28262	0.28219	-1.7	0.229
CC_05A II_48	863	28	0.28186	0.00008	0.000570	2.11E-05	0.28224	0.28262	0.28185	-13.9	0.971
CC_05A III_2	872	25	0.28219	0.00010	0.000876	8.09E-05	0.28223	0.28261	0.28218	-2.0	0.240
CC_05A II_18	873	27	0.28216	0.00008	0.000839	1.77E-05	0.28223	0.28261	0.28215	-3.0	0.155
CC_05A II_34	890	16	0.28215	0.00006	0.000571	3.13E-05	0.28222	0.28260	0.28214	-2.9	0.216
CC_05A II_30	910	28	0.28175	0.00009	0.000804	1.80E-05	0.28221	0.28259	0.28173	-16.9	0.905
CC_05A II_39	941	26	0.28213	0.00007	0.000638	5.40E-05	0.28219	0.28256	0.28212	-2.4	0.265
CC_05A II_19	943	16	0.28204	0.00009	0.001014	1.90E-05	0.28219	0.28256	0.28203	-5.7	0.208
CC_05A III_21	989	25	0.28224	0.00008	0.000730	1.24E-05	0.28216	0.28253	0.28223	2.5	0.105
CC_05A II_37	1044	23	0.28203	0.00009	0.001432	2.77E-05	0.28212	0.28249	0.28200	-4.3	0.179
CC_05A III_20	1052	23	0.28216	0.00008	0.001192	8.23E-05	0.28212	0.28248	0.28214	0.8	0.073
CC_05A II_41	1457	21	0.28146	0.00008	0.001322	4.21E-05	0.28186	0.28218	0.28142	-15.6	0.722
CC_05A III_13	1732	18	0.28173	0.00008	0.000890	3.19E-05	0.28168	0.28198	0.28171	0.9	0.041

APENDICE E

Dados in situ de zircão Lu-Hf da amostra CC_03B obtidos por LA-MC-ICP-MS.

			Sample (Present day ratios)						Sample Initial Ratios		
Name	U/Pb Age (Ma)	±2s	$^{176}Hf/^{177}Hf$ (t)	±2SE	$^{176}Lu/^{177}Hf$	±2SE	CHUR $^{176}Hf/^{177}Hf$ (t)	DM $^{176}Hf/^{177}Hf$ (t)	$^{176}Hf/^{177}Hf$ (t)	εHf(t)	±2SE
CC_03B 56	623	44	0.28209	0.00008	0.0003374	1.465E-05	0.28239	0.28280	0.28209	-10.7	1.23
CC_03B 57	633	28	0.28215	0.00007	0.0009991	3.845E-05	0.28239	0.28279	0.28214	-8.6	0.71
CC_03B 100	633	36	0.28252	0.00146	0.0004387	6.362E-05	0.28239	0.28279	0.28251	4.6	0.94
CC_03B 87	644	63	0.28208	0.00006	0.0003309	4.249E-06	0.28238	0.28278	0.28208	-10.7	1.19
CC_03B 99	663	41	0.28194	0.00008	0.0011057	2.047E-05	0.28237	0.28277	0.28193	-15.6	1.26
CC_03B 40	664	21	0.28182	0.00010	0.0016882	2.989E-05	0.28237	0.28277	0.28180	-19.9	0.98
CC_03B 132	666	18	0.28157	0.00008	0.0014483	2.564E-05	0.28236	0.28276	0.28155	-28.9	1.30
CC_03B 39	682	39	0.28235	0.00007	0.0009817	3.594E-05	0.28235	0.28275	0.28234	-0.6	0.05
CC_03B 10	683	26	0.28224	0.00008	0.0004050	2.498E-05	0.28235	0.28275	0.28223	-4.3	0.43
CC_03B 155	695	28	0.28200	0.00007	0.0009347	1.682E-05	0.28235	0.28274	0.28199	-12.7	0.74
CC_03B 37	746	15	0.28206	0.00009	0.0007046	2.750E-05	0.28231	0.28271	0.28205	-9.3	0.55
CC_03B 49	764	42	0.28249	0.00010	0.0005442	4.650E-05	0.28230	0.28269	0.28248	6.5	0.91
CC_03B 130	764	17	0.28218	0.00019	0.0007857	4.916E-05	0.28230	0.28269	0.28217	-4.8	0.41
CC_03B 12	777	54	0.28244	0.00009	0.0005092	5.448E-05	0.28229	0.28268	0.28243	4.8	0.86
CC_03B 20	780	27	0.28200	0.00009	0.0008820	2.089E-05	0.28229	0.28268	0.28199	-10.8	0.63
CC_03B 129	781	69	0.28211	0.00008	0.0007965	4.313E-05	0.28229	0.28268	0.28210	-6.7	0.96
CC_03B 50	854	70	0.28212	0.00010	0.0008110	3.924E-05	0.28224	0.28263	0.28211	-4.8	0.63
CC_03B 18	864	41	0.28210	0.00157	0.0008083	3.904E-05	0.28224	0.28262	0.28208	-5.5	0.56
CC_03B 65	868	53	0.28207	0.00010	0.0009805	3.634E-05	0.28224	0.28262	0.28206	-6.3	0.62
CC_03B 11	882	41	0.28206	0.00046	0.0016588	9.032E-05	0.28223	0.28261	0.28203	-7.1	0.72
CC_03B 91	883	43	0.28186	0.00010	0.0013311	3.345E-05	0.28223	0.28261	0.28184	-13.6	1.01
CC_03B 91	883	43	0.28208	0.00008	0.0009572	3.810E-05	0.28223	0.28260	0.28207	-5.6	0.50
CC_03B 66	891	44	0.28204	0.00008	0.0014212	5.267E-05	0.28222	0.28260	0.28201	-7.3	0.64
CC_03B 48	895	65	0.28212	0.00010	0.0008660	5.313E-05	0.28222	0.28260	0.28211	-3.9	0.53
CC_03B 63	960	45	0.28204	0.00034	0.0008030	2.748E-05	0.28218	0.28255	0.28202	-5.5	0.45
CC_03B 35	973	44	0.28204	0.00007	0.0006246	7.411E-06	0.28217	0.28254	0.28203	-5.0	0.29
CC_03B 59	1303	62	0.28224	0.00009	0.0011753	4.055E-05	0.28196	0.28229	0.28221	8.9	0.73
CC_03B 9	1439	49	0.28186	0.00008	0.0006117	1.305E-05	0.28187	0.28219	0.28184	-1.0	0.06
CC_03B 45	1581	49	0.28131	0.00011	0.0004139	1.728E-05	0.28178	0.28209	0.28129	-17.2	1.26
CC_03B 148	1838	36	0.28124	0.00055	0.0010641	1.929E-05	0.28161	0.28190	0.28120	-14.6	0.58